8-13-2019

Vision in an abundant North American bird: The Red-winged Blackbird

Esteban Fernández-Juricic
Purdue University, efernan@purdue.edu

Patrice E. Baumhardt
Purdue University

Luke P. Tyrrell
Purdue University & SUNY Plattsburgh

Amanda Elmore
Purdue University

Shelagh T. DeLiberto
USDA National Wildlife Research Center, shelagh.t.deliberto@aphis.usda.gov

The Auk
Ornithological Advances

AmericanOrnithology.org

Volume XX, 2019, pp. 1–27
DOI: 10.1093/auk/ukz039

RESEARCH ARTICLE

Vision in an abundant North American bird: The Red-winged Blackbird

Esteban Fernández-Juricic,[1,*] Patrice E. Baumhardt,[1] Luke P. Tyrrell,[1,2] Amanda Elmore,[1] Shelagh T. DeLiberto,[3] and Scott J. Werner[3]

[1]Department of Biological Sciences, Purdue University, West Lafayette, Indiana, USA
[2]Department of Biological Sciences, SUNY Plattsburgh, Plattsburgh, New York, USA
[3]United States Department of Agriculture, Animal Plant Health Inspection Service, Wildlife Services, National Wildlife Research Center, Fort Collins, Colorado, USA
*Corresponding author: efernan@purdue.edu

Submission Date: 21 September 2018; Editorial Acceptance Date: 7 May 2019; Published 13 August 2019

ABSTRACT

Avian vision is fundamentally different from human vision; however, even within birds there are substantial between-species differences in visual perception in terms of visual acuity, visual coverage, and color vision. However, there are not many species that have all these visual traits described, which can constrain our ability to study the evolution of visual systems in birds. To start addressing this gap, we characterized multiple traits of the visual system (visual coverage, visual acuity, centers of acute vision, and color vision) of the Red-winged Blackbird (*Agelaius phoeniceus*), one of the most abundant and studied birds in North America. We found that Red-winged Blackbirds have: wide visual coverage; one center of acute vision per eye (fovea) projecting fronto-laterally with high density of single and double cones, making it the center of both chromatic and achromatic vision; a wide binocular field that does not have the input of the centers of acute vision; and an ultraviolet sensitive visual system. With this information, we parameterized a Red-winged Blackbird-specific perceptual model considering different plumage patches. We found that the male red epaulet was chromatically conspicuous but with minimal achromatic signal, but the male yellow patch had a lower chromatic but a higher achromatic signal, which may be explained by the pigment composition of the feathers. However, the female epaulet was not visually conspicuous in both the chromatic and achromatic dimensions compared with other female feather patches. We discuss the implications of this visual system configuration relative to the foraging, antipredator, mate choice, and social behaviors of Red-winged Blackbirds. Our findings can be used for comparative studies as well as for making more species-specific predictions about different visual behaviors for future empirical testing.

Keywords: Agelaius phoeniceus, binocular vision, color vision, ultraviolet-sensitive, visual field

Visión de un ave abundante de América del Norte: Agelaius phoeniceus

RESUMEN

La visión de las aves es fundamentalmente diferente de la visión de los humanos; sin embargo, incluso entre las especies de aves hay diferencias substanciales en la percepción visual en términos de agudeza visual, cobertura visual y visión del color. Sin embargo, no hay muchas especies que tienen todos estos rasgos visuales descriptos, lo que puede restringir nuestra habilidad para estudiar la evolución de los sistemas visuales en las aves. Para comenzar a llenar este vacío, caracterizamos múltiples rasgos del sistema visual (cobertura visual, agudeza visual, centros de visión aguda, visión del color) de *Agelaius phoeniceus*, una de las aves más abundantes y estudiadas de América del Norte. Encontramos que *A. phoeniceus* tiene: amplia cobertura visual; un centro de visión aguda por ojo (fóvea) de proyección fronto-lateral con alta densidad de conos simples y dobles, convirtiéndolo en el centro tanto de la visión cromática como de la acromática; un campo binocular amplio que no tiene la entrada de los centros de visión aguda; y un sistema visual sensible a los rayos ultravioleta. Con esta información, parametrizamos un modelo perceptual específico para *A. phoeniceus* considerando diferentes parches del plumaje. Encontramos que la charretera roja del macho fue cromáticamente conspicua pero con una mínima señal acromática, y que el parche amarillo del macho tuvo una menor señal cromática pero una mayor señal acromática, lo que puede ser explicado por la composición del pigmento de las plumas. Sin embargo, la charretera de la hembra no fue visualmente conspicua tanto en la dimensión cromática como en la acromática comparada con otros parches de plumas de las hembras. Discutimos las implicancias de esta configuración del sistema visual en relación a los comportamientos de forrajeo, anti-depredador, de elección de pareja y social de *A. phoeniceus*. Nuestros resultados pueden ser usados para estudios comparativos, así como para hacer predicciones más específicas a nivel de especie sobre diferentes comportamientos visuales en futuras evaluaciones empíricas.

Palabras clave: Agelaius phoeniceus, campo visual, sensibilidad a los rayos ultravioleta, visión binocular, visión del color

INTRODUCTION

Visually, the way birds perceive the world is different from the way humans perceive the world. This is because birds generally have a wider color space due to 4 visual pigments in 4 types of single cone photoreceptors, a better ability to discriminate closely spaced wavelengths because of light filtering organelles in their cone photoreceptors (oil droplets), an extra cone type (double cone) apparently specialized in achromatic and motion vision, a wider visual coverage, and a quicker processing of images because of their higher temporal visual resolution (Martin and Osorio 2008, Hodos 2012, Tanaka 2015). Given these striking differences, some authors have called for taking a more bird-oriented sensory perspective when studying different aspects of their evolution, ecology, and behavior (Bennett et al. 1994, Endler and Mielke 2005).

However, one of the most interesting aspects of avian vision is the large degree of between-species variability in different visual dimensions: visual field configuration (Martin 2017); number, type, and position of the centers of acute vision (Fernández-Juricic 2012, Moore et al. 2016); absorbance properties of oil droplets (Hart and Hunt 2007, Toomey and Corbo 2017); relative densities of cone photoreceptors (Hart 2001b); and perception of chromatic signals (Fernández-Juricic 2016). This between-species variation has even been found in species that are closely related phylogenetically (but see Coyle et al. 2012). For instance, dabbling ducks (Family Anatidae) vary in the overall visual coverage (Guillemain et al. 2002). Sparrows (Family Emberizidae) vary in the size of the binocular field as well as the projection of their centers of acute vision (Moore et al. 2015). All in all, this between-species diversity in visual traits can influence visual perception (visual acuity and color vision) with the potential to affect behavior (Moore et al. 2017).

Characterizing key visual sensory dimensions of birds that could influence behavior is certainly relevant from a comparative point of view, such as understanding the evolution of the avian visual system. Yet few species have had their visual systems comprehensively characterized. We found only 5 bird species that have had all multiple visual traits (visual field configuration, visual acuity, density and distribution of cone photoreceptors and retinal ganglion cells, sensitivity of visual pigments, and absorbance of oil droplets) measured: American Goldfinch (*Spinus tristis*; Baumhardt et al. 2014), Brown-headed Cowbird (*Molothrus ater*; Blackwell et al. 2009, Fernández-Juricic et al. 2013, Goller et al. 2018), Canada Goose (*Branta canadensis*; Fernández-Juricic et al. 2011, Moore et al. 2012), European Starling (*Sturnus vulgaris*; Martin 1986, Hart et al. 1998, Dolan and Fernández-Juricic 2010), and Feral Pigeon (*Columba livia*; Binggeli and Paule 1969, Martin and Young 1983, Bowmaker et al. 1997, Querubin et al. 2009). Even a species often used in modeling color vision like the Blue Tit (*Cyanistes caeruleus*) still has some of these traits unmeasured (visual field configuration, density and distribution of retinal ganglion cells). This shortage of visual sensory information can also become an issue when it comes to interpreting the results of different behavioral studies (foraging, mate choice, and antipredator behavior) as sometimes incorrect assumptions are made about the way birds gather visual information (Fernández-Juricic et al. 2004, Fernández-Juricic 2012).

In this study, we characterized multiple traits of the visual system of the Red-winged Blackbird (*Agelaius phoeniceus*): eye size, ocular media transmittance, visual field configuration, retinal ganglion cell and single/double cone density and distribution, visual pigment sensitivity, and oil droplet absorbance. Red-winged Blackbirds belong to the Family Icteridae and Order Passeriformes, which has the highest number of extant avian species. These traits are relevant in explaining visual coverage (visual field configuration), visual acuity (eye size, density of retinal ganglion cells—neurons that connect the retina with the visual centers of the brain), projection of the centers of acute vision in the visual field (distribution of retinal ganglion cells and single/double cones), and color vision (ocular media transmittance, single/double cone density, visual pigment sensitivity, and oil droplet absorbance). With all this species-specific information, we estimated for the first time the degree of visual conspicuousness of male and female Red-winged Blackbird plumage patches from the visual point of view of Red-winged Blackbirds. These plumage patches are functionally relevant in the context of their social and breeding behavior (Searcy and Yasukawa 1995), making it more important to match species-level signals with species-level perception.

The Red-winged Blackbird is one of the most abundant birds in North America (Yasukawa and Searcy 1995). They are strongly polygynous and primarily granivorous, though they are also insectivorous during the breeding season (Yasukawa and Searcy 1995). Because of their conspicuous sexual dimorphism (males have more colorful plumage and are larger than females), Red-winged Blackbirds have long served as a model species for investigations on sexual selection and the evolution of ornamental traits (McGraw et al. 2004, Yasukawa et al. 2009a, 2009b, 2010). We discuss the implications of our visual system configuration results for different ecological aspects of this species (foraging, antipredator behavior, territory spacing, and signaling).

METHODS

A total of 22 Red-winged Blackbirds were used in this study (18 males, 4 females). Of these, 10 males were captured in

January 2015 in Weld County, Colorado, by the United States Department of Agriculture (USDA) Animal and Plant Health Inspection Service (APHIS) National Wildlife Research Center at Fort Collins, Colorado (hereafter called the 2015 Colorado bird pool). Immediately after capture, these Red-winged Blackbirds were transported to Purdue University in a van and housed together in a 1.83 × 1.83 × 3.66 m outdoor aviary at the Ross Biological Reserve, where they were provided with water, baths, and a food mix containing cracked corn, Purina gamebird chow, and dried mealworms ad libitum. These 10 individuals were then transported to the Purdue University campus immediately before being euthanized for physiological measurements. The remaining 12 birds were captured in 2010 (9 individuals; 7 males and 2 females) and 2013 (3 individuals; 1 male and 2 females) in Tippecanoe County, Indiana (hereafter known as the 2010 and 2013 Indiana bird pools, respectively). These 12 individuals were used for measurements of retinal ganglion cell density and visual field configuration only. Immediately after capture, these 12 individuals were housed indoors at the Purdue University campus on a 14:10 hour light-dark cycle in 0.61 × 0.61 × 0.76 m cages, where they were provided with water and cracked corn ad libitum. The difference in food provided to the 2 groups of birds was the result of changes in animal care protocols requiring a more balanced diet. All animal care, handling, transport, and euthanasia procedures were approved by the Purdue Animal Care and Use Committee (protocol 1201000567).

Eye Size

Prior to hemisecting the eyes for the different techniques (see details below), we measured eye axial length (width of eye from the surface of the cornea to the back of the eye [mm]), eye transverse diameter (diameter of the eye when viewing the front of the eye [mm]), and corneal diameter (diameter of the cornea in the sclerotic ossicles [mm]) with a caliper.

Ocular Media Transmittance

We measured the ocular media from 5 males (5 left and 5 right eyes; obtained from the 2015 Colorado bird pool). We hemisected the eyes of 2 males using a razorblade on the posterior surface of the eye to maintain the structure of the ocular media on the anterior segment of the eye following Hart et al. (2000a). The remaining 3 males were used for photoreceptor density and distribution measurements. For the hemisected eyes, the hemisection cut was made so that the opening on the back of the eye was the approximate size of the cornea (Hart et al. 2000a). We measured the transmittance of the intact ocular media of the hemisected eyes, vitreous humor, cornea, and lens in 1 nm increments from 300 to 700 nm using a StellarNet Black Comet spectroradiometer (StellarNet, Tampa, Florida, USA). Measurements were taken as quickly as possible (within 8–31 min of hemisection) as the ocular media tends to become opaque over time.

We placed the hemisected eye with phosphate buffered saline (PBS; to prevent desiccation and maintain eye cup structure) into a special eye holder similar in design to the one presented in Hawryshyn et al. (1985) (Appendix Figure 8) to facilitate proper optical alignment and measurement of the ocular media. This eye holder was then placed on a Corning (St. Louis, MO, USA).

Corning No. 1 22 × 30 mm glass slide and then inserted into a StellarNet TXF-1 transmission fixture. This fixture passes light from a StellarNet combination SL1+SL3 deuterium and tungsten halogen light source, through a 1,000 µm diameter fiber, to a set of 2 quartz collimating lenses, where the light is then sent to the spectrometer through another 1,000 µm diameter fiber (Appendix Figure 8). The eye holder and glass slide were placed and aligned in the light path between the 2 quartz collimating lenses within the fixture, allowing for light to pass through the cornea, lens, and vitreous humor of the hemisected eye, respectively (Appendix Figure 8). When possible, we also individually measured the components of the ocular media (cornea-lens, vitreous humor) in the same manner, but without using the eye holder as it was no longer needed to maintain proper alignment of these tissues in the transmission fixture. To calculate the transmittance of the ocular media from these tissue measurements, we took a baseline transmittance measurement after removing the tissue of interest from the light path and measuring how light traveled through the fixture. We then calculated the transmittance of the ocular media by taking the log of the tissue sample spectrum divided by the baseline spectrum at each wavelength (nm). We normalized the resulting spectra to 1 (100% transmittance) to determine the wavelength at which 50% of light was transmitted ($\lambda_{T0.5}$; Hart et al. 2000b, Hart 2004).

Visual Field Configuration

The visual field is the amount of space around the head an animal can see from. The visual field configuration refers to the size (in degrees [°]) of the binocular field, lateral fields, and blind area at different elevations around the head. We measured the visual field configuration of 10 Red-winged Blackbirds (6 males and 4 females from the 2010 and 2013 Indiana bird pools) using the ophthalmoscopic reflex technique (Hughes 1979) developed for visual field measurements by Martin (1984), which briefly consists of measuring the elevations around the head from which the retina reflects from a light source (Figure 1). We used 8 of the 10 individuals (5 males and 3 females from the 2010 and 2013 Indiana bird pools) for the at-rest measurements

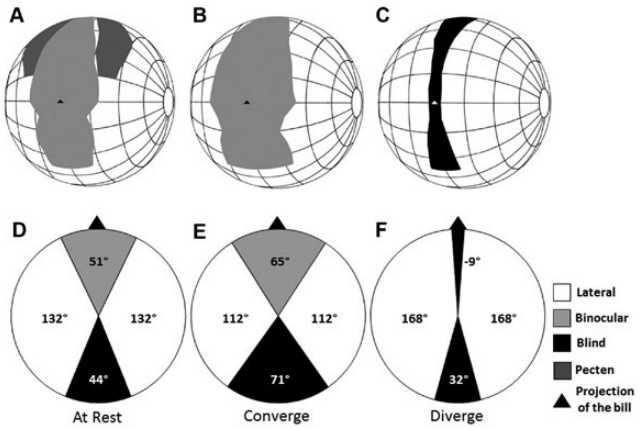

FIGURE 1. (**a**, **d**) Eyes at rest, (**b**, **e**) eyes converged, and (**c**, **f**) eyes diverged visual field configurations of the Red-winged Blackbird. (**a**–**c**) Spherical projection of the visual fields and pecten around the head of the bird. Lines correspond to latitude and longitude on a spherical coordinate system, which is centered on the head of the bird, in 20° increments. (**d**–**f**) Visual field configuration along the horizontal plane parallel to the ground (90–270°).

where the eyes were not moving (eye-resting position). While the eyes were at rest, we measured the extent of the pecten, which provides nourishment to the retina and creates a blind spot in the visual field (Raviola and Raviola 1967, Barlow and Ostwald 1972). We used 3 of the 10 individuals (1 male and 2 females from the 2013 Indiana bird pool) to measure the degree of eye movement when eyes were either converged toward or diverged from the front of the head.

We restrained individual birds in the center of the visual field apparatus with the beak held in place, at an angle consistent with the Red-winged Blackbird natural vigilance posture. This angle was determined using pictures of Red-winged Blackbirds in natural settings. The individual was held in a horizontal position inside a foam cradle. We measured the reflex of the retina at different positions around the head using an angular coordinate system, with the horizontal axis running directly through both eyes of the bird. The coordinate system begins directly above the head at 0°, progresses forward to the front of the head (90°), under the head (180°), around the back of the head (270°), and then ends directly above the head at 0° (aka 360°; Appendix Figure 11B). We called the plane that went parallel to the ground and through the subject's head (from the beak at 90° to the back of the head at 270°) the horizontal plane (Martin 2007). We used a Keeler Professional ophthalmoscope (accuracy of ± 0.5°) to measure the visual fields while the eyes were at rest, converged, and diverged in 10° increments around the head from 140° to 260° (Figure 1A–C). Due to the position of the body and the apparatus, we could not measure the extent of the visual field from 150° to 250° as the eyes were blocked at these angles. The converged and diverged eye movements were elicited by flashing lights or jingling keys around the individual. All measurements were corrected to account for the distance from the ophthalmoscope to the retina (Martin 1984). The sizes of the binocular, blind, lateral [360 – (mean blind + mean binocular visual fields)/2], and cyclopean (binocular + lateral right + lateral left visual fields) fields were calculated following Fernández-Juricic et al. (2008).

Retinal Ganglion Cell Density and Distribution

We extracted the eyes from 5 male Red-winged Blackbird individuals (from the 2010 Indiana bird pool) and measured eye axial length, corneal diameter, and transverse diameter. We hemisected the eyes to access the retina by cutting with a razorblade directly anterior to the ora serrata. Using a razorblade ensures a cleaner and safer cut than using a scalpel as in Stone (1981) and Baumhardt et al. (2014). We removed the vitreous humor using tweezers and spring scissors, then began removing the retina by severing the optic nerve and detaching the sclera from the choroidal layer as in Ullmann et al. (2012). Once the retina was extracted, we removed the excess pigmented epithelium with either a paintbrush or tweezers before we placed it in a solution of PBS (pH ~7.2–7.4, ~310 mOsm/kg) and 4% paraformaldehyde, being careful to ensure minimal mechanical damage of the retina during this process. After the retina was in this solution for 24 hr, it was removed, bathed in PBS, and placed into a 5% hydrogen peroxide bleaching solution for 5 days to remove any remaining pigmented epithelium.

After bleaching, we removed the retina, bathed it in PBS, and placed it on a gelatinized slide. We flattened the retina and removed the pecten to prevent asymmetrical shrinkage during the staining process (Stone 1981, Ullmann et al. 2012). We then took a picture of each retina using a Panasonic Lumix FZ28 camera to account for tissue shrinkage once stained. To attach the retina to the slide, we heat-fixed it at 60°C for 2 hr in a vessel containing 4 drops of formalin, and allowed it to sit in this vessel for an additional 24 hr. We then began the cresyl-violet staining process for each retina following the procedures of Stone (1981) and Ullmann et al. (2012), specifically following Table 1 in Ullmann et al. (2012) except with an additional 8 min in Histoclear for both steps 17 and 18. Once staining was complete, we covered the retina with Permount (Fisher Scientific, Waltham, MA, USA), added a coverslip on top, and let it dry. We then took an additional picture of the retina to measure the amount of tissue shrinkage that occurred. We measured the area of the retina using the before and after staining images with Image J (http://rsb.info.nih.gov/ij/).

We first visualized the whole-mounted, stained retina with a 4× objective and a 0.10 numerical aperture on an Olympus BX51 microscope (Olympus, Center Valley, PA,

TABLE 1. Mean wavelength at peak absorbance (λ_{max}) ± SE for the 4 single cone classes and 1 rod class of photoreceptors. Mean individual oil droplet spectral shape parameters ± SE (λ_{mid}, λ_{cut}, λ_0, b, and B_{mid}), and oil droplet average spectrum shape parameters (λ_{mid}, λ_{cut}, λ_0, b, and B_{mid}).

	Rod	Single cones				Double cones			
		UVS	SWS	MWS	LWS				
Visual pigments									
Mean λ_{max} of spectra (nm)	503 ± 0.57	384 ± 1.44	452 ± 1.70	503 ± 1.16	566 ± 2.31				
N	30	4	4	19	20				
		T-Type	C-Type	Y-Type	R-Type	P1-Type	P2-Type a	P2-Type b	P3-Type
Oil droplets									
Mean λ_{mid} (nm)			435 ± 1.22	537 ± 0.95	593 ± 0.63	452 ± 1.36	458 ± 0.80	501 ± 0.42	504 ± 0.54
Mean λ_{cut} (nm)			420 ± 1.03	516 ± 0.99	573 ± 0.71	430 ± 1.14	446 ± 1.42	486 ± 0.55	490 ± 0.63
Mean λ_0 (nm)			431 ± 1.13	532 ± 0.93	588 ± 0.63	446 ± 1.25	455 ± 0.94	497 ± 0.39	500 ± 0.54
Mean b			0.101 ± 0.0047	0.070 ± 0.0017	0.075 ± 0.0012	0.072 ± 0.0024	0.125 ± 0.0069	0.097 ± 0.0030	0.106 ± 0.0027
Mean B_{mid}			0.035 ± 0.0016	0.024 ± 0.00058	0.026 ± 0.00040	0.025 ± 0.00082	0.043 ± 0.0024	0.034 ± 0.0010	0.037 ± 0.00094
Mean absorbance spectrum									
λ_{mid} (nm)			433	535	591	447	458	499	502
λ_{cut} (nm)			418	516	573	427	446	487	489
λ_0 (nm)			429	530	586	442	455	496	499
B			0.098	0.074	0.08	0.071	0.123	0.116	0.115
B_{mid}			0.034	0.026	0.028	0.025	0.042	0.040	0.040
N		24	30	28	38	49	15		8

USA) and traced the perimeter of the retina with Stereo Investigator 9.13 (MBF Bioscience, Williston, VT, USA), which allows for the stereological estimation of retinal ganglion cell density. Using Stereo Investigator, we placed an orderly grid over the entire retina (Coimbra et al. 2009, Baumhardt et al. 2014). We used the SRS Image Series Acquire workflow to apply the orderly grid, which used the following parameters, as defined in West et al. (1991), Bonthius et al. (2004), and Baumhardt et al. (2014): area sampling fraction (asf; the ratio of the area of the counting frame to the area of the grid) = 0.009 ± 0.0004 per retina, ΣQ^- (the sum of the total number of neurons counted) = 14,212 ± 998 per retina, and thickness sampling factor (tsf; the ratio of the height of the dissector to the mean measured thickness) = 1 per retina. Stereo Investigator estimated that the average grid size, used for the retinas we counted, was 542.9 ± 11.5 × 543.4 ± 14.0 µm. Retinal ganglion cells were counted in a single layer as explained in Baumhardt et al. (2014).

Within each grid square on the retina, a 50 × 50 µm (0.0025 mm^2) counting frame was added on the upper left corner. We used this counting frame to prevent cell double counting. We used a 100x oil immersion objective and a 1.30 numerical aperture to find the plane with the highest contrast and resolution of cells that could be seen in fine focus. We took a picture of each counting frame with an Olympus S97809 microscope camera (Olympus) and then took a screen capture of each site using SnagIt (www.techsmith.com/Snagit). This allowed us to count the retinal ganglion cells within ImageJ (http://rsb.info.nih.gov/ij/). We counted cells that were within the counting frame and/or touched the upper and right edges of the frame, but did not count them if they were touching the lower and left edges of the frame (Gundersen 1977).

In some instances, a small portion of the counting frame encompassed areas where no ganglion cells were visible, either due to the counting frame being placed past the edge of the retina (at the tracing line), some cells being out of focus, or some patches containing pigmented epithelium. In these cases, we divided the counting frame into 4 separate quadrants, each 25 × 25 µm in size, which allowed us to count the retinal ganglion cells within the remaining quadrants contained inside the original counting frame. However, to avoid underestimating the density of cells at that grid site, we corrected for the reduced counting area during the cell density calculations following Dolan and Fernández-Juricic (2010).

Within the images we collected, other cell types were also stained with cresyl-violet, such as glial and amacrine cells. To address this issue, we identified retinal ganglion cells based on their cell shape, size of the soma, the accumulation of Nissl bodies in the cytoplasm, and the nucleus staining, as explained in detail in Baumhardt et al. (2014). We applied shrinkage corrections to each retina using the following formula: area of counting frame + (area of counting frame × proportion of shrinkage). This allowed us to calculate cell density (cells/mm^2) at each grid site by dividing the number of cells counted by the corrected tissue area (Baumhardt et al. 2014). The overall ganglion cell density was calculated considering all counting frames per retina, whereas the peak ganglion cell density was obtained from the counting frame with the highest cell density.

We calculated the total number of retinal ganglion cells N total = ΣQ^- × 1/asf × 1/tsf (following Coimbra et al. 2006). We also calculated the Scheaffer-Mendenhall-Ott coefficient of error (SMO CE) and the SMO CE^2/CV^2 (CV = coefficient of variation) ratio for each retina to verify the accuracy and reliability of our cell density estimations (see Results and Appendix Table 2; Glaser and Wilson 1998, Slomianka and West 2005, Baumhardt et al. 2014). We developed topographic maps of the variation in retinal ganglion cell density across the retina using isoclines that connect points with equal cell density (Figure 2). We developed the topographic maps with the R program called "One cell map V8 svg version 2," described in Garza-Gisholt et al. (2014).

The presence of a fovea was confirmed by identifying the location of a small invagination of the retinal tissue on each of the stained retinas and from a histological cross section of 2 Red-winged Blackbird retinas (from the 2013 Indiana bird pool). We performed this cross section by following the methods described in Tyrrell and Fernández-Juricic (2017a). Briefly, we hemisected the eye, fixed it in 4% paraformaldehyde, and took a 2 mm wide slice of the eye cup with the retina attached along the nasotemporal axis of the eye, ensuring that the fovea was centered within the slice. We then mounted the slice of the eye cup and retina in paraffin wax and sectioned it serially with a Thermo Scientific Shandon Finesse ME microtome (Waltham, Massachusetts, USA). We then stained the retinal sections with hematoxylin/eosin using a Thermo Scientific Shandon Varistain V24-3.

We calculated the peak and average visual acuity (cycles/degree) or anatomical spatial resolving power of the Red-winged Blackbird following Williams and Coletta (1987) and Pettigrew et al. (1988) and using this equation:

$$F_n = \sqrt{\frac{RMF}{2} \quad \frac{2D}{\sqrt{3}}}$$

where F_n is the highest spatial frequency that can be detected under optimal light conditions (Williams and Coletta 1987), the RMF is the retinal magnification factor calculated as $2\pi(PND)/360$ (Martin 1993, Ullmann et al. 2012), and D is the retinal ganglion cell density (Williams and Coletta 1987). We calculated visual acuity considering the overall as well as the peak retinal ganglion cell densities

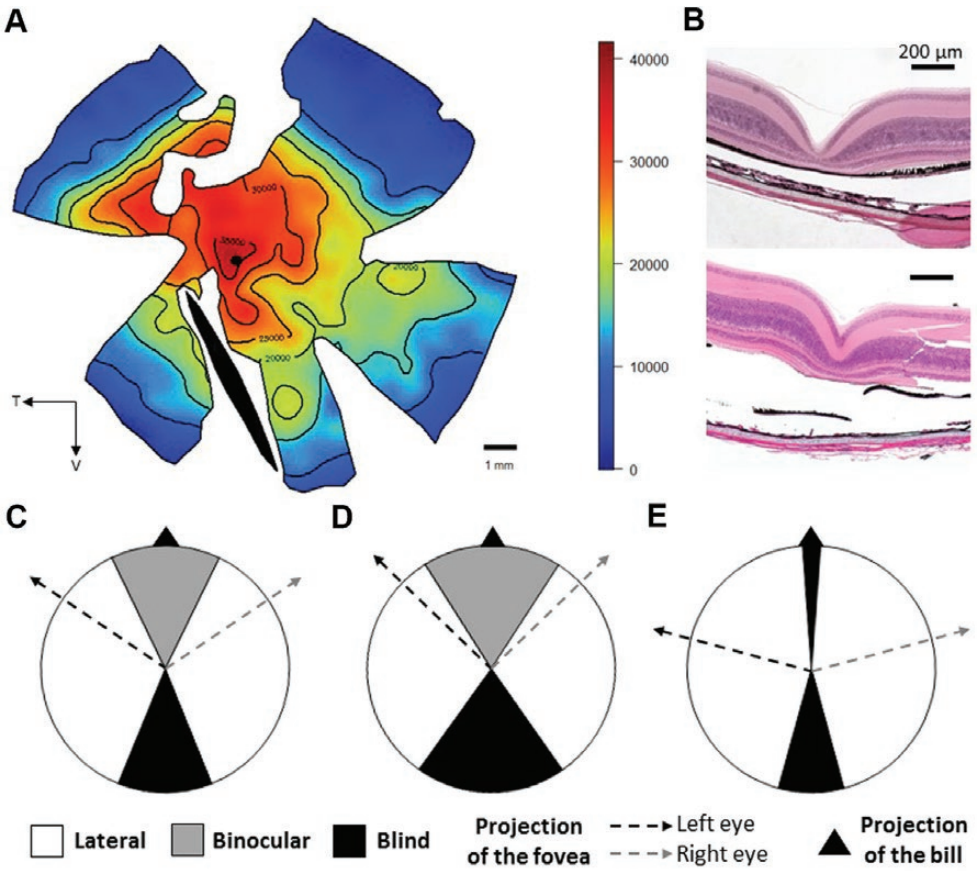

FIGURE 2. (**A**) Retinal ganglion cell topographic map of a Red-winged Blackbird retina. Isodensity lines connect areas of similar density (cells mm^{-2}) of retinal ganglion cells across the retina. T = Temporal; V = Ventral. The locations of the fovea and pecten are indicated by a black dot and a black streak, respectively. (**B**) Two individual cross sections showing the presence of a fovea (invagination of the retinal tissue) in the central part of the retina. Black scale bar is 200 µm. Projection of the fovea for left and right eyes in the visual field with eyes (**C**) at rest, (**D**) converged, and (**E**) diverged.

(Baumhardt et al. 2014, Moore et al. 2015). The posterior nodal distance (*PND*) was calculated by multiplying 0.67 by the eye axial length (following Pettigrew et al. 1988, Martin 1993, Ullmann et al. 2012).

Visual Pigment Sensitivity and Oil Droplet Absorbance

Four male Red-winged Blackbirds were used (from the 2015 Colorado bird pool) for microspectrophotometric measurements within 4 weeks of arrival to Purdue University. We dark-adapted by keeping individuals in a dark room for a 2–15 hr period to increase the concentration of visual pigment in the photoreceptors before tissue harvesting. We placed the first eye (alternating right or left between individuals) in PBS, which we then protected from light by covering the container in aluminum foil and placing it on ice. We hemisected the second eye at the ora serrata with a razorblade following the techniques explained in Ullmann et al. (2012). The vitreous humor was subsequently removed by cutting it away from the retina using small scissors. Using a small paintbrush, we carefully separated the retina from the back of the eye and floated it in a dish with PBS to prevent damage when cutting it. We cut 2–3 small ~8 mm^2 pieces of retinal tissue from the center and the periphery and placed them individually on Corning No. 1 22 × 30 mm glass slides. We chopped the small piece of retinal tissue into smaller pieces using a razorblade, placed a drop of PBS and a drop of sucrose water onto the tissue, covered it with a Corning No. 1 18 × 18 mm cover slip, and sealed the edges with black nail lacquer. The additional retinal preparations were stored in a refrigerator until use to reduce the amount of tissue degradation. All procedures and measurements took place in a dark room lit only by infrared or dim red lights so as not to bleach out the visual pigments.

We measured the absorbance of the oil droplets and visual pigments in the outer segments of cones and rods with a custom microspectrophotometer (MSP; Dr. Ellis Loew, Cornell University, Ithaca, New York, USA; McFarland and Loew 1994, Baumhardt et al. 2014). We

first isolated an area with individual outer segments and oil droplets, took a baseline measurement in a portion with no cells, then measured the absorbance of the nearby cell component at 1 nm intervals from 350 to 750 nm. If the cell measured was a suspected outer segment, we would then bleach the cell for a period of 60 s or more using white light to confirm the presence of a pigment and to distinguish it from other photo-reactive substances in the preparation (Liebman 1972). We only included in the analysis visual pigments that were successfully bleached. We distinguished medium-wavelength sensitive (MWS) outer segments from rod outer segments based on their physical characteristics: rod outer segments are large, long, and rectangular, with defined horizontal striations, whereas MWS outer segments are smaller, triangular, and have no noticeable striations (Crescitelli 1972). Oil droplets are easily visible and distinguishable by their spherical shape, so they do not need bleaching.

To determine the peak absorbance (λ_{max}) of the visual pigments, we created A1-rhodopsin templates of an ideal visual pigment spectrum using Govardovskii et al. (2000) equations 1, 2, 4, and 5. We then fitted these templates to the long-wavelength arm of the normalized visual pigment spectra measured in Microsoft Excel; hence, determining the wavelength (nm) at which the visual pigment is maximally sensitive to light for each spectrum (Figure 3).

To fully characterize the individual oil droplet spectra, 3 main parameters are determined: (1) λ_{cut}, the wavelength (nm) at which all light is absorbed by the oil droplet; (2) λ_{mid}, the wavelength (nm) at which 50% of the light is absorbed; and (3) λ_0, the wavelength (nm) at which 63% of the light is absorbed (where transmittance equals 1/*e*) (Lipetz 1984, Hart and Vorobyev 2005). We measured and calculated these 3 parameters for each oil droplet spectrum using OilDropSpec 4 (http://estebanfj.bio.purdue.edu/oildropspec), an oil droplet spectra analysis program for use with MATLAB (The MathWorks, Natick, Massachusetts, USA; Sesterhenn 2012, Ensminger et al. 2014). The program works by first normalizing the long-wavelength arm portion of the oil droplet spectra to 1. From this point, it determines λ_{mid}, fits a line on the spectra at 10 nm on both sides of the λ_{mid} point, and determines the slope, intercept, and R^2 value of the fitted line. Using this information, the program calculates the remaining oil droplet spectral shape parameters, λ_0, λ_{cut}, *b*, and β_{mid} (the last 2 parameters are related to the slope of the long-wavelength arm of the spectrum) following Hart and Vorobyev (2005). We also determined these spectral shape parameters for the average curve (all measured spectra averaged together) for each oil droplet type, following Hart (2004). Any oil droplet spectrum with a fitted line having an R^2 value of less than 0.5 was excluded from further analysis.

Photoreceptor Density and Distribution

All birds were dark adapted for 85–130 min before retinal extraction to facilitate removal of the pigmented epithelium from the retinal tissue. We extracted the retinae following the procedure described in the retinal ganglion cell section above on 4 male Red-winged Blackbirds (from the 2015 Colorado bird pool). We floated the retina onto a slide with PBS where it was flattened and then inverted it so that the photoreceptor layer was in the upper part of the slide. Any pigmented epithelium that remained attached to the retina was left in place to prevent mechanical damage to the cones. A coverslip was superglued to the slide to prevent desiccation during the photo acquisition period. A picture of the retina, once on the slide, was taken to verify retinal orientation.

We began the oil droplet counting process by visualizing the whole-mounted retina with a 4× objective and a 0.10 numerical aperture on an Olympus BX51 microscope (Olympus) and tracing the perimeter of the retina in Stereo Investigator 9.13 (MBF Bioscience). We used the SRS Image Series Acquire workflow to apply the orderly grid. This grid used the following parameters: asf = 0.005 ± 0.0004 per retina, ΣQ^- = 14,125 ± 941 per retina, tsf = 1 per retina. The average grid size determined by Stereo Investigator was 761.0 ± 2.3 × 730.0 ± 70.0 µm. Within each grid square on the retina, a 50 × 50 µm (0.0025 mm^2) counting frame was added on the upper left corner. We used a 40× objective to find the plane at which the most oil droplets could be seen in focus. We took a picture of each counting frame with an Olympus S97809 microscope camera (Olympus) under brightfield and epifluorescent lights. Exposure to the epifluorescent light was limited as much as possible to prevent bleaching of the oil droplets. We took screen captures of these images using SnagIt so that we could count the oil droplets within ImageJ. We counted oil droplets within the counting frame in the same manner as the retinal ganglion cells described above.

Based on the results from the microspectrophotometry section above, we found 5 distinct types of oil droplets, which were highly colored and easily distinguishable in the bright field (Y- and R-Types) or were only distinguishable in the epifluorescent (T-, C-, and P-Types). We used oil droplet type criteria to distinguish the 5 different types of oil droplets following Hart (2001b) and Baumhardt et al. (2014). We counted sites in which the tissue was undamaged from the retinal extraction process, was not folded or distorted, and contained no burst oil droplets or remaining pigmented epithelium. Once counting was completed, we calculated the cell density (cells/mm^2) at each grid site by dividing the number of cells counted by the counting frame area (Baumhardt et al. 2014). We calculated the total number of photoreceptors (N total), SMO CE, and the SMO CE^2/CV^2 ratio for each retina, as detailed

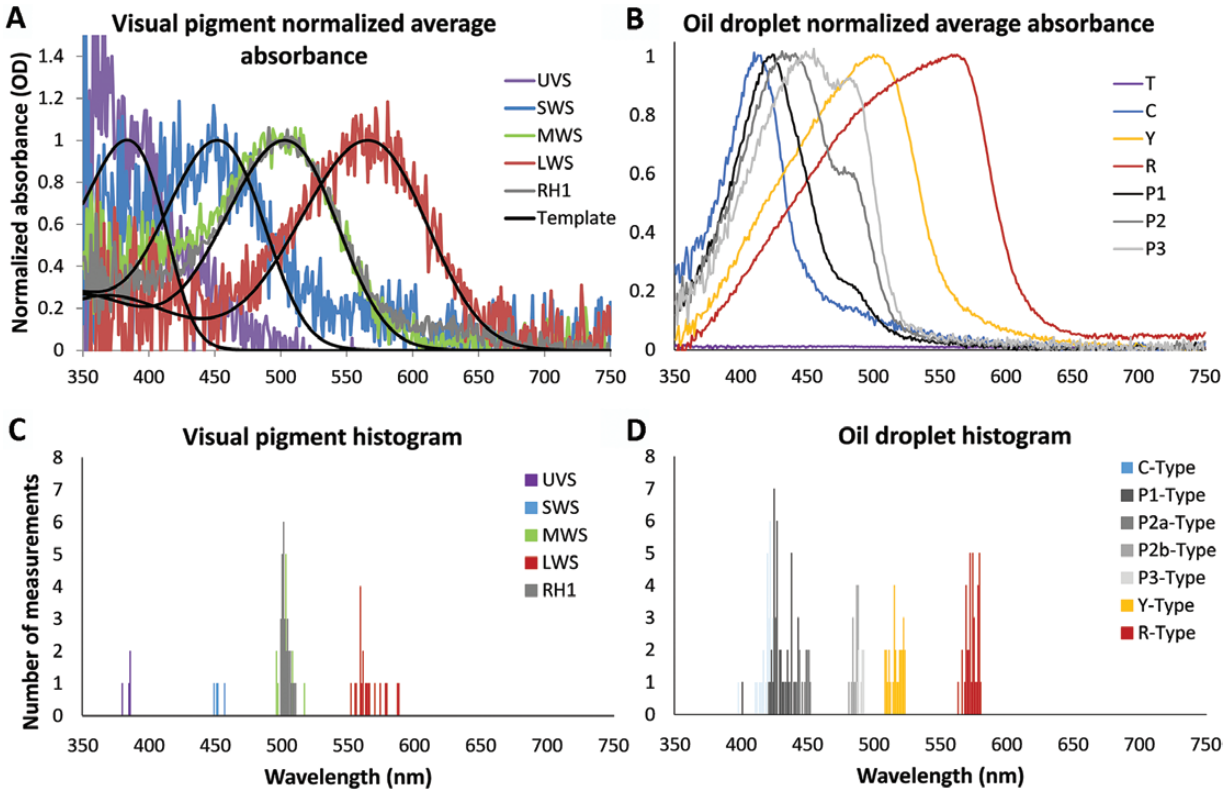

FIGURE 3. Microspectrophotometrically measured visual pigments and oil droplets of the Red-winged Blackbird. **(A)** Averaged normalized visual pigment spectra of the four single cones (UVS, SWS, MWS, and LWS) and the average normalized rod visual pigment (RH1) with the black lines indicating the A1-rhodopsin templates from Govardovskii et al (2000). (**B**) Averaged normalized oil droplet spectra of the four types of single cones (T-Type, C-Type, Y-Type, and R-Type), and the averaged normalized double cone with all P-Type variants measured (P1-Type, P2-Type, and P3-Type). (**C**) Histogram of the λ_{max} values for the single cone visual pigments (UVS, SWS, MWS, and LWS) and the rod (RH1) visual pigment. (**D**) Histogram of the λ_{cut} values for the single cone oil droplets (C-Type, Y-Type, and R-Type) and the double cone oil droplet with all three variants (P1-Type, P2-Type [a and b peaks], and P3-Type).

in the retinal ganglion cell section to verify the reliability of our counts (Appendix Table 2; Glaser and Wilson 1998, Slomianka and West 2005, Baumhardt et al. 2014).

For each retina, we created 6 topographic maps of the variation in cone density across the retina using isoclines that connect points with equal cell density based on each separate oil droplet type associated with the different cones (T-Type, C-Type, Y-Type, R-Type, and P-Type) as well as the sum of all cone types (Total) on the retina using an R program called "One cell map V8 svg version 2" (Garza-Gisholt et al. 2014). We overlaid a series of concentric rings on each of the 3 counted retinas in order to characterize the pattern of change in cone density (concentric increase). We determined the size of these rings by first calculating the proportional area of the highest density isocline (≥60,000 cells mm^{-2} for 2 retinas; ≥50,000 cells mm^{-2} for the third retina) in the topographic map including all cone types. We then used the average proportional area of highest density isocline to determine the area of a circle centered on the estimated location of the fovea (determined using the whole-mounted stained retinas described in the retinal ganglion cell section). We then set the width of 5 additional concentric rings around the fovea by using the diameter of this circle.

Perceptual Modeling of Plumage Patches

To estimate the degree of visual conspicuousness of the male and female plumage patches from the avian visual perspective, we used perceptual modeling. The model estimates in the chromatic and achromatic dimensions the degree of visual contrast of an object (plumage) relative to the visual background (vegetation). More specifically, we used Vorobyev and Osorio's receptor noise limited model to calculate chromatic and achromatic contrast (Vorobyev and Osorio 1998). This model requires the use of spectral data from 3 main components: the ambient light of the environment (absolute irradiance), the reflectance of the object of interest and the reflectance of the visual background, and species-specific data on the visual system (cone sensitivity and relative cone densities). The information gathered in the previous sections allowed us to calculate for the first time the chromatic and achromatic

contrasts specifically from the Red-winged Blackbird visual perspective. We determined how different plumage patches on the male and female Red-winged Blackbirds contrasted against vegetation (green grass). This simulates a scenario in which individuals are separated by a distance (e.g., distance between 2 territory holders) in which the visual angle is such that the vegetation occupies a larger proportion of the visual field.

We measured the reflectance of green grass in an open grassy field in West Lafayette, Indiana, USA (40.417370, –86.941781) on June 9, 2016. We took 21 reflectance measurements of the grass with a JAZ portable spectrometer (Ocean Optics, Dunedine, Florida, USA) from 300 to 700 nm, averaged and interpolated the data into 1 nm increments, then calculated the percent reflectance of the averaged grass spectrum. In both scenarios, we used ambient light data collected from an open grassy field on June 9, 2016 at 0920 hours (UTC-05:00) on a partly cloudy day (35% cloud cover). These data were collected using the absolute irradiance function on a JAZ portable spectrometer from 300 to 700 nm. We took 10 samples of the ambient light, 2 from each of the 4 cardinal directions and 2 directly up at the sky, at breast height. We averaged together the 10 irradiance spectra, converted the data from μWatt/cm^2/nm to μmol/s/m^2, and interpolated the data to 1 nm increments.

We measured the reflectance of the Red-winged Blackbird plumage in 3 males (from the 2015 Colorado bird pool) and 1 female (from the 2013 Indiana bird pool) using a StellarNet Black Comet Spectroradiometer in 1 nm increments from 300 to 700 nm. We took 3 measurements, averaged them together, and calculated the percent reflectance for each of the beak, belly, breast, crown, mantle, dorsal side of tail feathers, ventral side of tail feathers, red epaulet, yellow epaulet/wing bar, the distal side of the flight feathers, and the proximal side (underside closest to body) of the flight feathers plumage patches on the male Red-winged Blackbird (Appendix Figure 9). We took 3 measurements, averaged them together, and calculated the percent reflectance for each of the beak, belly, breast, crown, mantle, dorsal side of tail feathers, ventral side of tail feathers, epaulet, the distal side of the flight feathers, and the proximal side of the flight feathers, cheek, eye bar, and throat plumage patches on the female Red-winged Blackbird. We used the male and female plumage patches as the object of interest and the grass leaves as a background in the contrast model. The percent reflectance is the ratio of the reflectance of the plumage and the reflectance of an ideal standard under the same light source, with the area under the percent reflectance curve indicating the lightness of the plumage patch (Andersson and Prager 2006). The percent reflectance spectra (rather than colorimetric parameters) are used in the calculation of visual contrast.

To make the visual contrast models Red-winged Blackbird-specific, we calculated the wavelength-specific photon capture probability (C_r (λ); Figure 4E, F; equation 8 in Endler and Mielke 2005) for each photoreceptor by creating templates of each visual pigment normalized absorbance (G_r (λ) parameter) (using λ_{max}; Figure 4A, B; Govardovskii et al. 2000) and the corresponding oil droplet transmittance (T_{or} (λ) parameter) (using λ_{cut} and B_{mid}; Figure 4C; equation 17 in Hart and Vorobyev 2005). We also used TableCurve 2D (Systat Software, San Jose, CA, USA) to fit a curve to the average hemisected eye ocular media transmittance curve (T_e (λ) parameter) (Figure 4D). We used the resulting wavelength-specific photon capture probability spectra (Figure 4E, F) and the cone photoreceptor relative densities (including the double cone) in the model. We used the vismodel and coldist functions with a weber fraction of 0.1 in Pavo 1.0, as explained in Maia et al. (2013), to estimate chromatic and achromatic contrasts. We calculated achromatic contrast separately from chromatic contrast by using the short-wavelength sensitive (SWS), MWS, long-wavelength sensitive (LWS), and double cone sensitivity curves in the *visual* argument within the vismodel function, and the SWS, MWS, LWS, and double cone relative densities in the *n* argument within the coldist function, as recommended (R. Maia personal communication). The output of the contrast calculations is in units of just noticeable differences (JND), with a JND of more than 4 being considered that the animal can easily distinguish the object from the visual background (Siddiqi et al. 2004).

RESULTS

Eye Size

We measured 3 eye size parameters on 13 males. The mean (± SE) eye axial length was 8.11 ± 0.11 mm, transverse eye diameter was 9.94 ± 0.05 mm, and corneal diameter was 5.97 ± 0.06 mm.

Ocular Media Transmittance

We measured 4 hemisected eyes (2 right, 2 left) from 2 males (hemisection opening dimensions = 7.57 ± 0.75 × 7.55 ± 0.74 mm). We also measured the individual ocular media components from 5 eyes (2 right, 3 left) of 3 males. The average $\lambda_{T0.5}$ (the wavelength at which 50% of light was transmitted) values were as follows: hemisected eye = 324 ± 6.40 nm (Appendix Figure 10A); cornea-lens = 323 ± 8.11 nm; and vitreous humor = 360 ± 28.87 nm (Appendix Figure 10B). We could not separate the cornea from the lens without complete destruction of the tissues, so we measured them together.

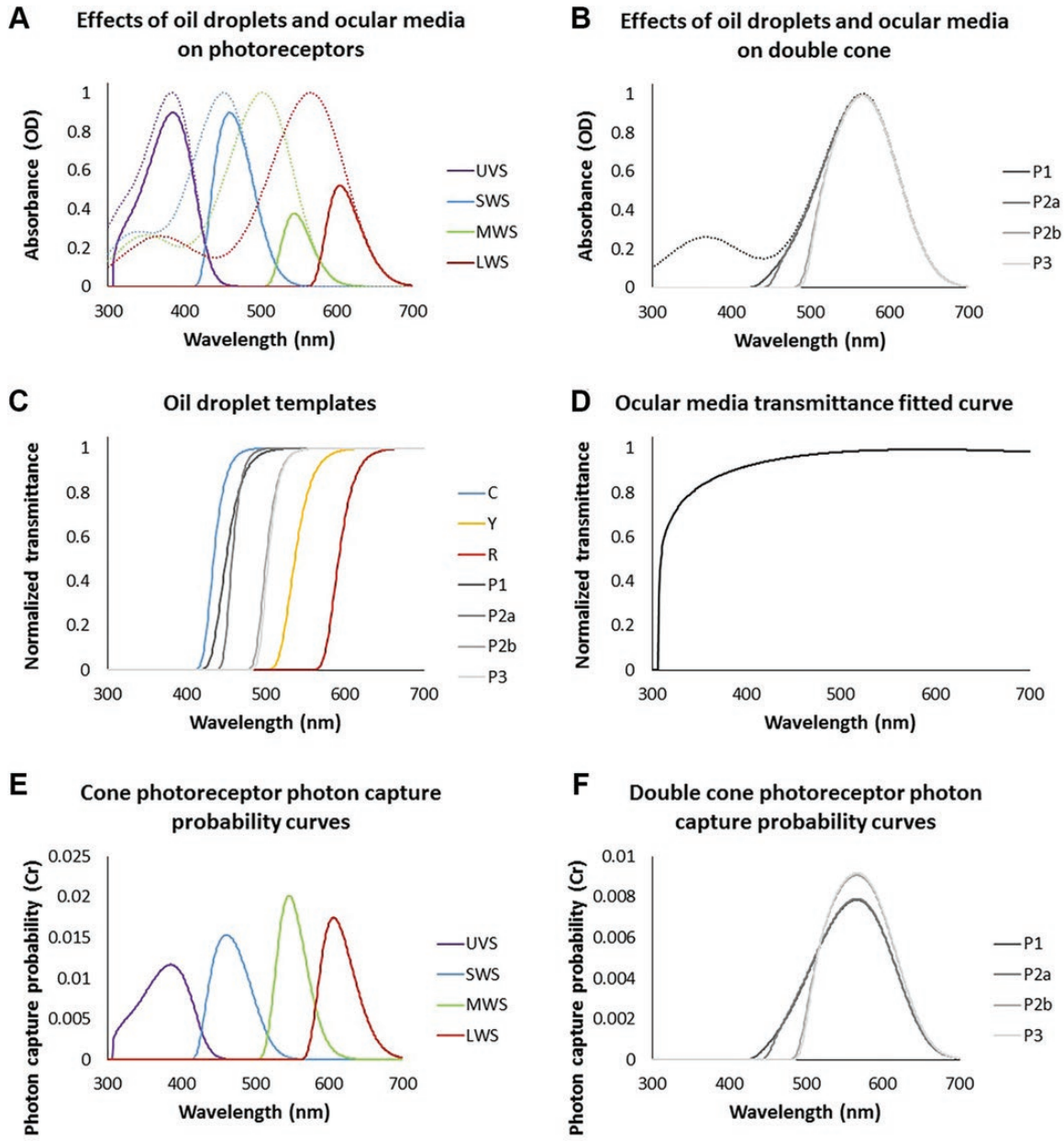

FIGURE 4. Predicted sensitivity of the Red-winged Blackbird cone photoreceptors and spectra used in the calculation of the wavelength-specific photon capture probability (C_r (λ)). (**A**) and (**B**) Predicted sensitivity of the cone photoreceptors considering (1) the spectral tuning effects of the oil droplets and ocular media for the 4 single cones, and (2) the spectral tuning of the double cone with all P-Type variants, as in Hart and Vorobyev (2005). Dotted lines represent the visual pigment template for each specific photoreceptor, with the double cone using the LWS pigment, used in the calculation of the wavelength-specific photon capture probability (C_r (λ)), as in Endler and Mielke (2005). (**C**) Normalized oil droplet transmittance templates from each single cone oil droplet type and all double cone P-Type variants used in the calculation of the wavelength-specific photon capture probability (C_r (λ)). (**D**) Normalized transmittance of the hemisected eye ocular media fitted curve used in the calculation of the wavelength-specific photon capture probability (C_r (λ)). (**E**) and (**F**) Resulting wavelength-specific photon capture probability (C_r (λ)) spectra for (**E**) each single cone photoreceptor, and (**F**) the double cone photoreceptor with all P-type variants used in the contrast calculations.

Visual Field Configuration

We found that the beak extends into the binocular field of the Red-winged Blackbird, as evidenced by the beak obstructing the visual field between 90° and 110° elevations (see indentations in binocular field Figure 1A, B). This indicates that individuals are able to see the tip of their beaks when their eyes are at rest or converged (Figure 1A, B). The width of the binocular field at the horizontal

plane was 51.46 ± 2.89° with the eyes at rest, with a maximum width of 52.08 ± 2.13° at the 80° elevation (Figure 1A, D). The average width of the binocular field across all elevations was 34.81 ± 3.39° with the eyes at rest, extending from 0° (top of head) vertically to 140° (below the beak) (Figure 1A). The width of the blind area at the horizontal plane was 44.15 ± 2.71° with the eyes at rest (Figure 1D), with a maximum of 63.54 ± 2.20° at the 250° elevation. The average width of the blind area across all elevations was 30.34 ± 5.87° with the eyes at rest. The size of the lateral field at the horizontal plane was 132° with the eyes at rest (Figure 1D), consequently the cyclopean field (lateral right and left fields + binocular field) was 316°. The average width of the lateral field and cyclopean fields (in the 70–140° elevations where we were able to collect information from both the binocular and blind areas) were 139.70 ± 4.03° and 321.52 ± 5.64°, respectively (Figure 1A). The average width of the pecten, whose projection creates a blind spot in the visual field, across all elevations measured was 19.44 ± 1.32° with the eyes at rest. The pecten extended from 0° (top of head) vertically to 70° (dorsal to the beak) (Figure 1A).

We found that Red-winged Blackbirds can move their eyes considerably, but differently depending on the elevation along the head (Appendix Figure 11A, B). The largest degree of eye movement (36.90 ± 1.15°) was measured at 90° along the horizontal plane (Appendix Figure 11B). The average amplitude of eye movement across all elevations measured was 28.64 ± 3.26°.

On the horizontal plane, the width of the binocular field and blind area increased by 14° and 27°, respectively, when the eyes converged relative to the eyes at rest position (Figure 1B, E). The width of the cyclopean field decreased by 27° when the eyes converged (Figure 1E). On the horizontal plane, the width of the binocular field decreased by 60° when the eyes diverged, leading to a 9° blind area in front of the head (Figure 1C, F). On the horizontal plane, the width of the blind area decreased by 12° when the eyes diverged (Figure 1F).

Retinal Ganglion Cell Density and Distribution

We used 5 eyes from 5 males (3 right, 2 left eyes). Out of the average 412.4 ± 2.5 number of grid sites photographed per retina, we were able to count an average of 365.4 ± 7.9 grid sites per retina. The average amount of retinal shrinkage for these retinas was 1.2 ± 0.3%. We found that the mean density of the retinal ganglion cells was 15,498 ± 955 cells mm^{-2} for the whole retina, with a peak density of 41,061 ± 2,735 cells mm^{-2}. The estimated total number of cells on the retina was 1,664,799 ± 83,217 cells. The average SMO CE was 0.028 ± 0.0008, which was highly reliable as it was well below the 0.1 threshold (Glaser and Wilson 1998, Slomianka and West 2005, Coimbra et al. 2009). The average SMO CE^2/CV^2 ratio was 0.002 ± 0.00005, below the 0.5 threshold set by Slomianka and West (2005), indicating that our counts were highly reliable estimates of cell density. The topographic maps showed a region of high density (≥35,000 cells mm^{-2}) slightly off, dorso-temporally, the center of the retina (Figure 2A). We confirmed that Red-winged Blackbirds had a single fovea per retina as their center of acute vision given the invagination of the retinal tissue around the area with the highest cell density (Figure 2B). The fovea projected fronto-laterally with the eyes at rest (Figure 2C), but did not enter the binocular field even when the animals converged their eyes (Figure 2D). From the fovea, the ganglion cell density decreased concentrically towards the periphery of the retina (Figure 2A). Based on eye size and ganglion cell density, we estimated the peak and average visual acuity of the Red-winged Blackbird to be 9.22 ± 0.23 and 5.72 ± 0.25 cycles/degree, respectively.

Visual Pigment Sensitivity and Oil Droplet Absorbance

We were able to measure visual pigment sensitivity from 47 cones and 30 rods from 4 males. The visual pigments of the cone and rod photoreceptors were confirmed to be A1-rhodopsin pigments during the template-fitting process (Govardovskii et al. 2000). Red-winged Blackbirds, like other bird species, have 4 classes of single cones, 1 class of double cone, and 1 class of rod (Figure 3A) photoreceptors. The mean peak absorbance (λ_{max}) values of the single cone visual pigments were estimated as: 384 ± 1.44 nm (ultraviolet wavelength sensitive [UVS]; range: 380–386 nm, with lambda max values of 380 nm, 385 nm, 386 nm, and 386 nm for each of the individual cones measured), 452 ± 1.70 nm (SWS), 503 ± 1.16 nm (MWS), and 566 ± 2.31 nm (LWS) (Table 1; Figure 3A, C; Appendix Figure 13). The double cone visual pigment could not be found during the data collection period. The peak absorbance (λ_{max}) of the rod photoreceptor was estimated as 503 ± 0.57 nm (rhodopsin [RH1]) (Table 1; Figure 3A, C; Appendix Figure 13). An individual exemplar UVS visual pigment, post-bleach and rotated spectrum, and difference spectrum can be viewed in Appendix Figure 14. The apparent mismatch between the peak of the raw data relative to the peak of the fitted curve is because of the noisy nature of the UVS visual pigment data; however, we followed the template-fitting process (Govardovskii et al. 2000) to establish the peak absorbance (λ_{max}), as described in the Methods section. The naming of photoreceptors and visual pigments followed the convention of Hart (2001a), as we did not have the facilities to perform genetic tests to distinguish between SWS1 and SWS2 opsins.

We were able to measure oil droplet absorbance from 192 oil droplets from the same 4 males. We identified 5 main types of oil droplets: T-Type, associated with the UVS

single cone; C-Type, associated with the SWS single cone; Y-Type, associated with the MWS single cone; R-Type, associated with the LWS single cone; and P-Type, associated with the double cone. The P-Type oil droplet contained 3 variants (P1-Type, P2-Type, and P3-Type) likely due to differences in carotenoid concentration (Table 1; Figure 3B, D; Appendix Figure 13). The fact that we found P-Type oil droplets confirms that Red-winged Blackbirds have double cones (Hart 2001a), despite the fact that we could not find the visual pigment associated with these double cones (see previous paragraph). The P2-Type contains a double peak, which had to be analyzed separately; therefore, we called the higher absorbance peak P2(a) and the lower absorbance peak P2(b) (Figure 3B, D). The P1- and P2-Type variants were found throughout the retina, while the P3-Type variant was only found in the periphery of the retina. The mean λ_{cut} of single cone oil droplets were estimated as: 420 nm (C-Type [SWS]), 516 nm (Y-Type [MWS]), and 573 nm (R-Type [LWS]) (Table 1). The mean λ_{cut} estimates for double cone oil droplets were: 430 nm (P1-Type), 446 nm (P2-Type; a peak), 486 nm (P2-Type; b peak), and 490 nm (P3-Type) (Table 1; Figure 3B, D; Appendix Figure 13). The remaining spectral shape parameters (λ_{mid}, λ_0, b, and β_{mid}) for all of the oil droplet types are listed in Table 1, except the T-Type oil droplet since it is transparent and has no absorbance properties above 300 nm (Hart 2001a).

We calculated the peak sensitivity of the photoreceptor visual pigments including the effects of the ocular media and oil droplet transmittance following equation 17 in Hart and Vorobyev (2005) and equation 1 in Govardovskii et al. (2000) (Figure 4A, B). These calculations are relevant because they consider the visual signal generated at the level of the photoreceptor after other optical effects are factored in. The peak sensitivity (λ_{max}) of the visual pigment is therefore changed: in the UVS cone from 384 to 385 nm, in the SWS cone from 452 to 460 nm, in the MWS cone from 503 to 544 nm, and in the LWS cone from 566 to 605 nm (Figure 4A). The λ_{max} of the double cone does not change as a result of the ocular media and oil droplet transmittance (Figure 4B).

Photoreceptor Density and Distribution

We used 3 eyes from 2 males (1 right, 2 left eyes). Out of the average 280.7 ± 23.2 number of grid sites collected per retina, we were able to count an average of 188.3 ± 20.2 grid sites per retina. The average SMO CE was 0.019 ± 0.0012 and the average SMO CE^2/CV^2 ratio was 0.002 ± 0.0002, well below the 0.1 and 0.5 thresholds, respectively, indicating that our cell density estimates were highly reliable (Glaser and Wilson 1998, Slomianka and West 2005, Coimbra et al. 2009). We estimated the mean density of all cone types (based on oil droplets) as 30,373 ± 551 cells mm^{-2} for the whole retina, with a peak density of 66,000 ± 7,111 cells mm^{-2}. The mean density of all single cone photoreceptors involved in color vision (UVS, SWS, MWS, and LWS) was 16,970 ± 360 cells mm^{-2}, and that of the double cone photoreceptor involved in achromatic vision was 13,402 ± 252 cells mm^{-2}. The mean density per cone photoreceptor type was: UVS (T-Type oil droplet) = 2,496 ± 63 mm^{-2}; SWS (C-Type oil droplet) = 5,586 ± 149 mm^{-2}; MWS (Y-Type oil droplet) = 4,365 ± 104 mm^{-2}; LWS (R-Type oil droplet) = 4,523 ± 88 mm^{-2}; double cone (P-Type oil droplet) = 13,402 ± 252 mm^{-2}. The relative densities of Red-winged Blackbird cone photoreceptors (used in perceptual modeling) were: 1 (UVS): 2.24 (SWS): 1.75 (MWS): 1.81 (LWS): 5.37 (double cone). The estimated total number of all cones, single cones, and double cones across the whole retina were: 3,097,611 ± 75,041, 1,742,178 ± 107,051, and 1,355,433 ± 37,566 cells, respectively.

The density of both single and double cones showed a consistent pattern of concentric increase from the retinal periphery towards the foveal area as shown in the density plots considering different concentric rings centered around the fovea (Figure 5) as well as in the topographic maps (Appendix Figure 12). The area with the highest density of both single and double cones (Appendix Figure 12) coincides with the position of the fovea established from examination of the retinal ganglion cell layer (Figure 2).

Additionally, we sorted out the cone densities in 2 portions of the retina: the foveal area, which projects into the fronto-lateral portion of the visual field (Figure 2C), and the temporal area, which projects into the binocular field (Figure 2C). The density of all single cones (ANOVA, $F = 48.23$, df = 1 and 149, $P < 0.001$) and double cones (ANOVA, $F = 28.87$, df = 1 and 149, $P < 0.001$) was significantly higher in the foveal area (single cones, 31,656 ± 2,266 cells mm^{-2}; double cones, 19,256 ± 1,266 cells mm^{-2}) than the temporal area (single cones, 15,346 ± 606 cells mm^{-2}; double cones, 12,207 ± 338 cells mm^{-2}), as expected. However, the ratio of double to single cones was significantly higher (ANOVA, $F = 5.84$, df = 1 and 149, $P = 0.017$) in the temporal area (0.95 ± 0.03) than in the foveal area (0.62 ± 0.13).

Perceptual Modeling of Plumage Patches

Our visual contrast model with Red-winged Blackbird-specific visual sensory information provided a picture of what parts of the male and female plumage are more visually conspicuous from the visual perspective of conspecifics. When different plumage patches were contrasted against the surrounding vegetation, the male red epaulet was by far the most chromatically conspicuous patch, followed by the distal side of the flight feathers, crown, and top of the tail (Figure 6A). Achromatically, however, Red-winged Blackbirds would have a challenging time discriminating the male red epaulet from the visual background given its

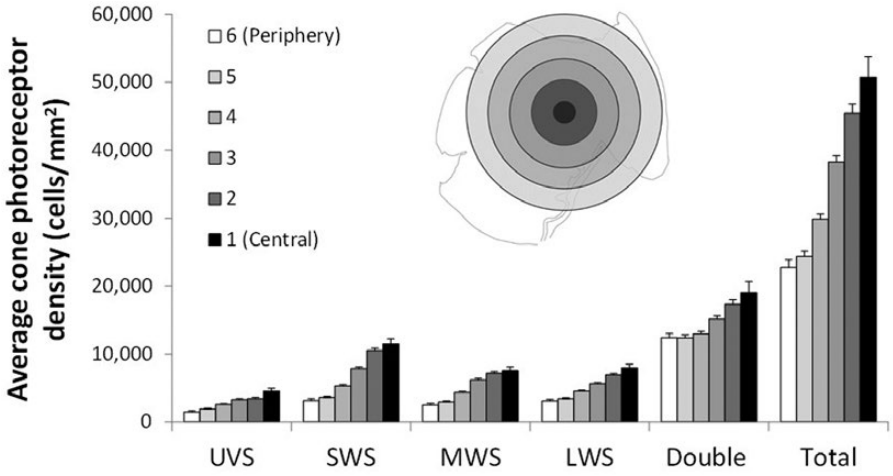

FIGURE 5. Average (± SE) density of cone photoreceptors (UVS, SWS, MWS, LWS, double cone, and total) across the retina shown in concentric rings of similar width (from (1) centrally located circle centered on the fovea to (6) retinal periphery). (Inset) Small diagram shows an example of concentric ring configuration.

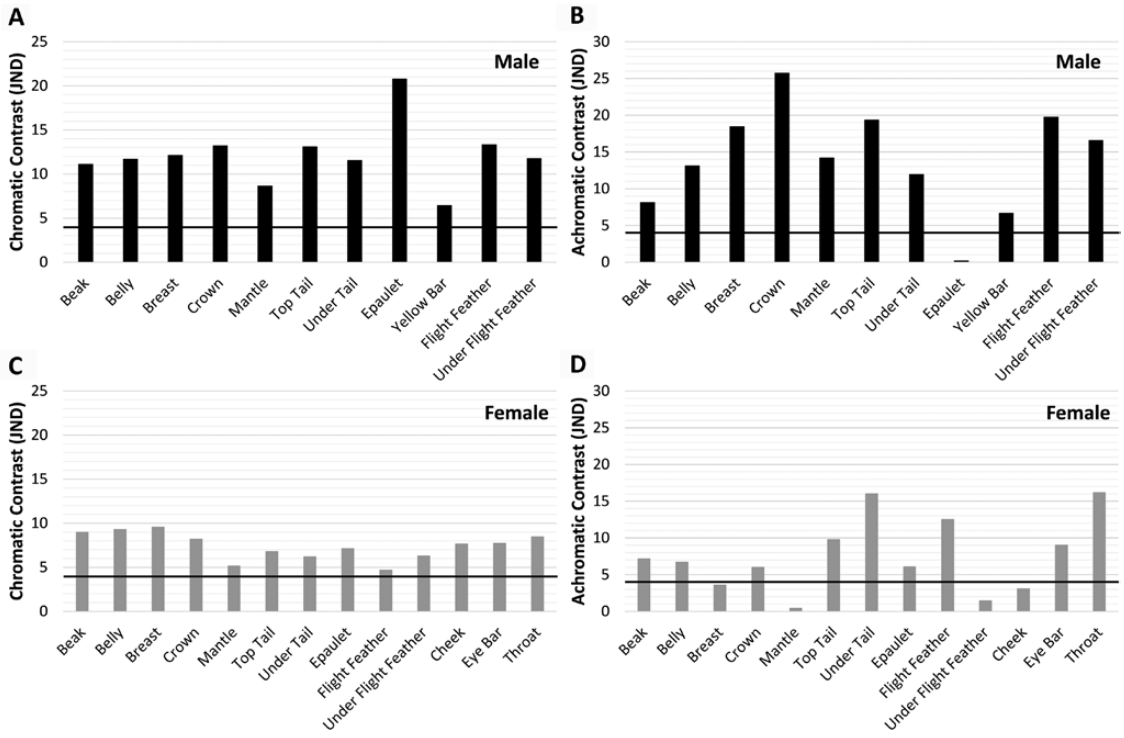

FIGURE 6. Chromatic (**A, C**) and achromatic (**B, D**) contrast of plumage patches against grass leaves for the male (**A, B**) and female (**C, D**) Red-winged Blackbird main plumage patches: beak, belly, breast, cheek (female only), crown, epaulet, eye bar (female only), flight feather (distal side of flight feathers), mantle, tail (dorsal side of tail feathers), throat (female only), under flight feather (proximal side of flight feathers), under tail (ventral side of tail feathers), and yellow wing bar (male only) (see Appendix Figure 9).

low values. However, the crown, distal side of the flight feathers, top of the tail, and breast had the highest achromatic conspicuousness (Figure 6B). Females, in contrast, were chromatically much less conspicuous than males overall from the visual perspective of the species, with throat, breast, belly, and beak as the most visually conspicuous (Figure 6C). From an achromatic perspective, female under-tail, distal side of the flight feathers and throat were

the most conspicuous patches relative to the visual background of the vegetation (Figure 6D).

DISCUSSION

Red-winged Blackbirds have relatively wide visual coverage, a single center of acute vision per eye (fovea) projecting fronto-laterally, a concentric increase in the density of both retinal ganglion cells and cones towards the center of acute vision, a relatively wide binocular field that does not have foveal input, and an ultraviolet sensitive visual system. In general terms, the Red-winged Blackbird visual configuration bears a lot of similarities with that of the American Goldfinch (Baumhardt et al. 2014), Brown-headed Cowbird (Blackwell et al. 2009, Fernández-Juricic et al. 2013), and European Starling (Martin 1986, Hart et al. 1998, Dolan and Fernández-Juricic 2010). We discuss these findings from both behavioral and ecological perspectives.

Red-winged Blackbirds have visual coverage similar to other passerine birds (blind area ~40°; Moore et al. 2015, Tyrrell and Fernández-Juricic 2017a). This large visual coverage means that they should be able to gather information about foraging opportunities (conspecifics finding food) as well as potential risks (predators attacking, conspecifics escaping) from their lateral fields even when their heads are down in a putatively foraging posture, as other passerine birds do (Fernández-Juricic et al. 2008). Nevertheless, there are 2 interesting sensory input constraints in the blackbird visual field configuration. The vertical length of the binocular field seems limited above and below the beak (Figure 7A) compared with other passerine birds (Fernández-Juricic et al. 2008, Baumhardt et al. 2014, Moore et al. 2015). Thus, Red-winged Blackbirds would not be able to get much visual input right above and behind their heads given their visual field configuration (Figure 7A, B). Additionally, their pectens generate a blind spot on each side of the binocular field in the upper part of the visual field (Figure 7C, D). This may limit their ability to detect aerial predator attacks along the median plane particularly when their heads are down while foraging (Figure 7C) or displaying visual signals (Figure 7D), but the large lateral visual coverage especially when diverging the eyes may partially compensate for this constraint (Figure 1F). Furthermore, the binocular field projection below the head does not reach the ground (Figure 7A), as in other passerine birds (e.g., House Sparrow [*Passer domesticus*], House Finch [*Haemorhous mexicanus*]; Fernández-Juricic et al. 2008). Therefore, Red-winged Blackbirds may not be able to see the ground when head-up (Figure 7A), limiting the gathering of foraging information to head-down body postures (Figure 7B).

The density of single and double cones was substantially higher around the foveal area than the rest of the retina. Thus, the fovea in Red-winged Blackbirds can be considered the center of both chromatic and achromatic vision, as is the case of other passerine birds (Baumhardt et al. 2014). The implication is that after detection and when exploring visually specific targets (conspecifics), Red-winged Blackbirds are expected to use to a large extent their foveae to resolve as much detail as possible. Given that their foveae project fronto-laterally, high-acuity visual exploration would take the form of rapid lateral head movements to fixate with either laterally placed eye aligned with the object of interest. Actually, our estimates of peak visual acuity (9.22 cycles per degree around the center of acute vision) allow us to calculate the spatial scales the Red-winged Blackbird eye can reach under hypothetically perfect illumination conditions (see Tyrrell et al. 2013 for formulas). Additionally, the distance at which an object is resolved may not necessarily be the same at which an object is recognized as belonging to a certain category (conspecific, predator). Thus, these distances are expected to be overestimates. For instance, a Red-winged Blackbird should be able to resolve a conspecific (22 cm length; Yasukawa and Searcy 1995) from 232 m, and the red epaulet of a male (4.37 cm length; Eckert and Weatherhead 1987) from 46.12 m. The red epaulet of male Red-winged blackbirds is a threat and dominance signal between rival males (Smith 1972). Interestingly, the diameter of an average Red-winged Blackbird territory is ~50 m (Yasukawa and Searcy 1995), suggesting that to assess the variation in epaulet size (Røskaft and Rohwer 1987, Yasukawa et al. 2009b), neighbor males would need to position themselves within a relatively reduced spatial window (<50 m).

From an antipredator perspective, the key is the detection of a visual stimulus that could have characteristics (due to motion, size, coloration, contrast) suggesting a potential predator. This first detection can occur with any portion of the retina and is followed by visual exploration with the fovea in the direction of the stimulus (Sokolov et al. 2002). Given that any part of the retina could be involved in the first detection, we used the average visual acuity estimate (5.72 cycles per degree) to calculate the distances that the Red-winged Blackbird could detect its main known adult and egg predators (Bird 1930, Yasukawa and Searcy 1995) under hypothetically perfect illumination conditions (see Tyrrell et al. 2013 for formulas). Considering terrestrial predators (averaged body lengths obtained from animaldiversity.org), Red-winged Blackbirds should be able to resolve raccoons (*Procyon lotor*, 77.7 cm) from 509 m, and American minks (*Neovison vison*, 61 cm) from 400 m. Considering aerial predators (averaged body lengths obtained from animaldiversity.org), Red-winged Blackbirds should be able to resolve Cooper's Hawks (*Accipiter cooperii*, 42.5 cm) from 279 m, Sharp-shinned

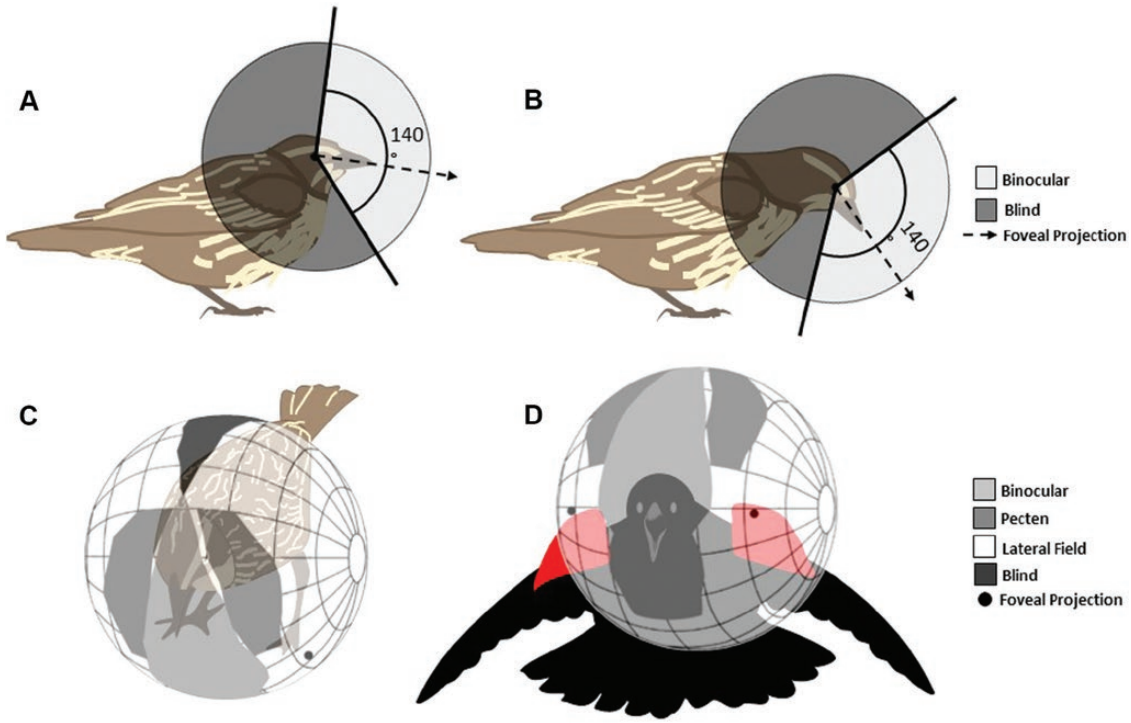

FIGURE 7. The projection of the visual fields on Red-winged Blackbird males (**D**) and females (**A–C**) during behaviorally and ecologically relevant body postures and activities. (**A**) Vertical length of the binocular (light grey) and blind area (dark grey) and projection of the fovea (dashed arrow) while foraging in the head-up body posture. (**B**) Vertical length of the binocular (light grey) and blind area (dark grey) and projection of the fovea (dashed arrow) while foraging in the head-down body posture. (**C**) Spherical projection of the visual fields (binocular [grey], lateral [white], and blind [black]), pecten (dark grey) and foveae (black circles) into the visual space around the head of a foraging head-down body posture. (**D**) Spherical projection of the visual fields (binocular [grey], lateral [white], and blind [black]), pecten (dark grey) and foveae (black circles) into the visual space around the head during a male display.

Hawks (*Accipiter striatus*, 29 cm) from 190 m, Black-billed Magpies (*Pica hudsonia*, 52.5 cm) from 344 m, and Marsh Wrens (*Cistothorus palustris*, 12.2 cm) from 80 m. Thus, if the 2 aforementioned hawks were to initiate an attack on an adult bird, Red-winged Blackbirds would have 21 s and 14 s after detection, respectively, to escape successfully based on the averaged flight speeds of these raptors (Broun and Goodwin 1943).

Red-winged Blackbirds have relatively wide binocular fields that they can widen even more by converging their eyes towards their bills due to their degree of eye movement. Furthermore, their foveae do not project into the binocular field, even when the eyes are converged. The implication is that visual perception around the Red-winged Blackbird bill varies from binocular vision to high acute vision on the right and left sides of the edges of the binocular field. This is likely to influence its visual exploration strategy while foraging. Sideways head exposures to the substrate may provide high ability to resolve stimuli both chromatically and achromatically, whereas exposing the bill towards the substrate may provide 2 visual inputs (though of lower spatial resolving power than those of the foveae) that may enhance contrast discrimination (Heesy 2009). Binocular vision in birds is not well understood from a functional perspective (Martin 2009, Tyrrell and Fernández-Juricic 2017b); however, an interesting finding was that the ratio of double to single cones was higher in the portion of the retina subtending the binocular field than that subtending the foveal field. Previous studies in humans have drawn functional implications based on variations in the ratios of cone photoreceptors (Cicerone 1990). Along these lines, our findings suggest that in Red-winged Blackbirds achromatic vision may be of higher relevance in the binocular field than in the foveal field. This idea could be tested in the future using behavioral assays that consider the projection of the foveal and binocular fields described in this study.

Based on microspectrophotometric data, we found that Red-winged Blackbirds are sensitive to the ultraviolet portion of the spectrum (UVS visual system), as suggested by Aidala et al. (2012) based upon DNA sequencing of the SWS1 photoreceptor. Additionally, Chen et al. (1984) and Chen and Goldsmith (1986) provided electrophysiological evidence for retinal cones that are maximally sensitive to

370 nm, 480 nm, and 570 nm in Red-winged Blackbirds. Their estimates of the sensitivity of the UVS, SWS, and LWS cones were off by 15, 20, and 35 nm, respectively, which is expected as electrophysiological measurements of cone sensitivity are not as accurate as microspectrophotometric ones. We compiled information from the literature on different visual dimensions associated with avian color vision (sensitivity of the UVS, SWS, MWS, and LWS cones, the transmittance of the ocular media, and the absorbance of the different types of oil droplets) from the species of birds studied so far (Appendix Figure 13). Along each of these dimensions, we plotted the reported values highlighting where the Red-winged Blackbird falls along the continuum. The Red-winged Blackbird appears to have intermediate values for most of these dimensions with the exception of the ocular media transmission (relatively low values), absorbance of the Y-type oil droplet (relatively high values), and absorbance of the P3 type oil droplet (relatively high values) (Appendix Figure 13). Overall, color vision in this species seems to be bounded by visual system sensitivities akin to previously studied bird species.

By collecting information on the sensitivity of the cone photoreceptors and their relative densities, we were able to model for the first time the degree of conspicuousness of different elements of the Red-winged Blackbird plumage along the chromatic and achromatic dimensions from the visual perspective of this species. Our results corroborate that even from an avian visual perspective, the plumage of males is more visually conspicuous both chromatically and achromatically than that of the females (Figure 6), giving females a high level of crypsis. Considerable research has emphasized the relevance of the red epaulets in males for territory establishment, defense, and mate attraction (Peek 1972, Eckert and Weatherhead 1987, Røskaft and Rohwer 1987, Yasukawa 2009a, 2009b, 2010). Considering vegetation as the visual background (when a male is in his territory looking at a neighbor at some distance), the visual conspicuousness of the red epaulet was found to be mostly chromatic with actually minimal conspicuousness in the achromatic dimension. On the other hand, the male's yellow patch generated a lower chromatic but a higher achromatic signal than the red epaulet. This difference may be explained by the pigment composition of the feathers. The color of the red epaulet comes from a combination of ketocarotenoids and eumelanins, whereas that of the yellow patch comes from mostly phaeomelanins with no carotenoids (McGraw et al. 2004). The reduction in the achromatic conspicuousness of the red epaulet may serve visual signaling purposes by over-emphasizing one visual dimension above the other. This finding has some future experimental design implications as any artificial manipulation of the degree of redness of the epaulet should ensure that it is not generating any achromatic signal residue.

Female Red-winged Blackbirds also have epaulets, but they vary substantially in brightness (Payne 1969), which has been associated with body condition (Johnsen et al. 1996) and age (Blank and Nolan 1983). Considering vegetation as the visual background, we found that the female epaulet was not visually contrasting (from a Red-winged Blackbird visual perspective) in both the chromatic and achromatic dimensions. In fact, there were other female feather patches that were more conspicuous than the epaulet (breast in the chromatic dimension, under tail in the achromatic dimension). The brightness of female epaulets seems to signal status in female-female aggressive encounters (Johnsen et al. 1996), which occur at close distances and thus may reduce the need for signaling from far away, as the males do. Additionally, given that the female epaulet is in a similar location to that of the male, females signaling may be taking advantage of an intrinsic species-bias in males and females to pay visual attention to that part of the body.

Besides the value of our findings for future comparative studies on the evolution of the avian visual system (Martin 2009, Coyle et al. 2012, Moore et al. 2017), we think these data can provide some perspective on previous studies and inform future research on the ecology and behavior of Red-winged Blackbirds. For instance, Red-winged Blackbirds forage in groups during the non-breeding season and some social foraging theoretical models make specific assumptions about the way group mates visually perceive predators and conspecifics (Fernández-Juricic et al. 2004). Our visual field configuration and visual acuity results can inform these models to make more blackbird-specific predictions that can be tested empirically. Red-winged Blackbirds have been the subject of a lot of mate choice and sexual selection work, with visual signaling being an important component (Searcy and Yasukawa 1995). The data on color vision (sensitivity of visual pigments, absorbance of oil droplets, and relative densities of cones) can be used to model the perception of Red-winged Blackbird visual signals and displays from the perspective of its own species. Red-winged Blackbirds can also produce considerable damage to crops (Linz et al. 2017). Our findings on the position of the centers of acute vision, size of the binocular field, and color vision can shed some new light as to the visual cues Blackbirds may be using to assess the foraging suitability of different crops depending on phenology. Overall, we believe that bringing the visual sensory perspective to this highly studied species can be of benefit from both theoretical and applied perspectives.

ACKNOWLEDGMENTS

We thank B. F. Blackwell, T. L. DeVault, D. C. Eckery and C. S. Olson for their thoughtful review of an early draft of

this manuscript. We also thank D. A. Reid for help with the logistics.

Funding statement: This project was partially funded by the National Science Foundation, the United States Department of Agriculture (USDA) National Wildlife Research Center (NWRC; Fort Collins, Colorado, USA), and Arkion Life Sciences (New Castle, Delaware, USA). Corporate collaborations do not imply endorsement by USDA or Purdue University.

Ethics statement: All animal care, handling, transport, and euthanasia procedures were approved by the Purdue Animal Care and Use Committee (protocol 1201000567).

Author contributions: E.F-J., P.E.B., S.T.D., and S.J.W. conceived the idea, design, experiment (supervised research, formulated question or hypothesis). E.F-J., P.E.B., S.T.D., L.P.T., and A.E. performed the experiments (collected data, conducted the research). E.F-J., P.E.B., S.T.D., and S.J.W. wrote the paper (or substantially edited the paper). E.F-J., P.E.B., and L.P.T. developed or designed methods. E.F-J. and P.E.B. analyzed the data. E.F-J. and S.J.W. contributed substantial materials, resources, or funding.

LITERATURE CITED

Aidala, Z., L. Huynen, P. L. Brennan, J. Musser, A. Fidler, N. Chong, G. E. Machovsky Capuska, M. G. Anderson, A. Talaba, D. Lambert, and M. E. Hauber (2012). Ultraviolet visual sensitivity in three avian lineages: Paleognaths, parrots, and passerines. Journal of Comparative Physiology. A, Neuroethology, Sensory, Neural, and Behavioral Physiology 198:495–510.

Andersson, S., and M. Prager (2006). Quantifying colors. In Bird Coloration: Mechanisms and Measurements, Vol. 1 (G. E. Hill and K. J. McGraw, Editors). Harvard University Press, Cambridge, UK. pp. 41–89.

Barlow, H. B., and T. J. Ostwald (1972). Pecten of the pigeon's eye as an inter-ocular eye shade. Nature: New Biology 236:88–90.

Baumhardt, P. E., B. A. Moore, M. Doppler, and E. Fernández-Juricic (2014). Do American Goldfinches see their world like passive prey foragers? A study on visual fields, retinal topography, and sensitivity of photoreceptors. Brain, Behavior and Evolution 83:181–198.

Beason, R. C., and E. R. Loew (2008). Visual pigment and oil droplet characteristics of the Bobolink (*Dolichonyx oryzivorus*), a new world migratory bird. Vision Research 48:1–8.

Bennett, A. T. D., I. C. Cuthill, and K. J. Norris (1994). Sexual selection and the mismeasure of color. American Naturalist 144:848–860.

Binggeli, R. L., and W. J. Paule (1969). The pigeon retina: Quantitative aspects of the optic nerve and ganglion cell layer. The Journal of Comparative Neurology 137:1–18.

Bird, R. D. (1930). Biotic communities of the Aspen Parkland of central Canada. Ecology 11:356–442.

Blackwell, B. F., T. L. DeVault, T. W. Seamans, S. L. Lima, P. Baumhardt, and E. Fernández-Juricic (2012). Exploiting avian vision with aircraft lighting to reduce bird strikes. Journal of Applied Ecology 49:758–766.

Blackwell, B. F., Fernández-Juricic, E., Seamans, T. W., and Dolan, T. (2009). Avian visual system configuration and behavioural response to object approach. Animal Behaviour 77:673–684.

Blank, J. L., and V. Nolan Jr (1983). Offspring sex ratio in Red-winged Blackbirds is dependent on maternal age. Proceedings of the National Academy of Sciences USA 80:6141–6145.

Bonthius, D. J., R. McKim, L. Koele, H. Harb, B. Karacay, J. Mahoney, and N. J. Pantazis (2004). Use of frozen sections to determine neuronal number in the murine hippocampus and neocortex using the optical disector and optical fractionator. Brain Research. Brain Research Protocols 14:45–57.

Bowmaker, J. K. (1979). Visual pigments and oil droplets in the pigeon retina, as measured by microspectrophotometry, and their relation to spectral sensitivity. In Neural Mechanisms of Behavior in the Pigeon (A. M. Granda and J. H. Maxwell, Editors). Plenum, New York, NY, USA. pp. 287–305.

Bowmaker, J. K., and G. R. Martin (1978). Visual pigments and colour vision in a nocturnal bird, *Strix aluco* (Tawny Owl). Vision Research 18:1125–1130.

Bowmaker, J. K., and G. R. Martin (1985). Visual pigments and oil droplets in the penguin, *Spheniscus humboldti*. Journal of Comparative Physiology A 156:71–77.

Bowmaker, J. K., J. K. Kovach, A. V. Whitmore, and E. R. Loew (1993). Visual pigments and oil droplets in genetically manipulated and carotenoid deprived quail: A microspectrophotometric study. Vision Research 33:571–578.

Bowmaker, J. K., L. A. Heath, S. E. Wilkie, and D. M. Hunt (1997). Visual pigments and oil droplets from six classes of photoreceptor in the retinas of birds. Vision Research 37:2183–2194.

Broun, M., and B. V. Goodwin (1943). Flight speeds of hawks and crows. The Auk 60:487–492.

Carvalho, L. S., B. Knott, M. L. Berg, A. T. D. Bennett, and D. M. Hunt (2011). Ultraviolet-sensitive vision in long-lived birds. Proceedings of the Royal Society B: Biological Sciences 278:107–114.

Chen, D. M., and T. H. Goldsmith (1986). Four spectral classes of cone in the retinas of birds. Journal of Comparative Physiology. A, Sensory, Neural, and Behavioral Physiology 159:473–479.

Chen, D. M., J. S. Collins, and T. H. Goldsmith (1984). The ultraviolet receptor of bird retinas. Science (New York, N.Y.) 225:337–340.

Cicerone, C. M. (1990). Color appearance and the cone mosaic in trichromacy and dichromacy. In Color Vision Deficiencies (Y. Ohta, Editor). Kugler & Ghedini, Amsterdam, The Netherlands.

Coimbra, J. P., M. L. Videira Marceliano, B. L. Da Silveira Andrade-Da-Costa, and E. S. Yamada (2006). The retina of Tyrant Flycatchers: Topographic organization of neuronal density and size in the ganglion cell layer of the Great Kiskadee *Pitangus sulphuratus* and the Rusty Margined Flycatcher *Myiozetetes cayanensis* (Aves: Tyrannidae). Brain, Behavior and Evolution 68:15–25.

Coimbra, J. P., N. Trévia, M. L. Marceliano, B. L. da Silveira Andrade-Da-Costa, C. W. Picanço-Diniz, and E. S. Yamada (2009). Number and distribution of neurons in the retinal ganglion cell layer in relation to foraging behaviors of Tyrant Flycatchers. The Journal of Comparative Neurology 514:66–73.

Coyle, B. J., N. S. Hart, K. L. Carleton, and G. Borgia (2012). Limited variation in visual sensitivity among bowerbird species suggests that there is no link between spectral tuning and

variation in display colouration. The Journal of Experimental Biology 215:1090–1105.

Crescitelli, F. (1972). The visual cells and visual pigments of the vertebrate eye. Handbook of Sensory Physiology 2:245–363.

Das, D., S. E. Wilkie, D. M. Hunt, and J. K. Bowmaker (1999). Visual pigments and oil droplets in the retina of a passerine bird, the Canary *Serinus canaria*: Microspectrophotometry and opsin sequences. Vision Research 39:2801–2815.

Dolan, T., and E. Fernández-Juricic (2010). Retinal ganglion cell topography of five species of ground-foraging birds. Brain, Behavior and Evolution 75:111–121.

Eckert, C. G., and P. J. Weatherhead (1987). Ideal dominance distributions: A test using Red-winged Blackbirds (*Agelaius phoeniceus*). Behavioral Ecology and Sociobiology 20:43–52.

Endler, J. A., and P. W. Mielke (2005). Comparing entire colour patterns as birds see them. Biological Journal of the Linnean Society 86:405–431.

Ensminger, A. L., and E. Fernández-Juricic (2014). Individual variation in cone photoreceptor density in House Sparrows: Implications for between-individual differences in visual resolution and chromatic contrast. Plos One 9:e111854.

Fernández-Juricic, E. (2012). Sensory basis of vigilance behavior in birds: Synthesis and future prospects. Behavioural Processes 89:143–152.

Fernández-Juricic, E. (2016). The role of animal sensory perception in behavior-based management. In Conservation Behaviour: Applying Behavioural Ecology to Wildlife Conservation and Management (D. Saltz and O. Berger-Tal, Editors). Cambridge University Press, Cambridge, UK.

Fernández-Juricic, E., J. T. Erichsen, and A. Kacelnik (2004). Visual perception and social foraging in birds. Trends in Ecology & Evolution 19:25–31.

Fernández-Juricic, E., M. D. Gall, T. Dolan, V. Tisdale, and G. R. Martin (2008). The visual fields of two ground-foraging birds, House Finches and House Sparrows, allow for simultaneous foraging and anti-predator vigilance. Ibis 150:779–787.

Fernández-Juricic, E., B. A. Moore, M. Doppler, J. Freeman, B. F. Blackwell, S. L. Lima, and T. L. DeVault (2011). Testing the terrain hypothesis: Canada geese see their world laterally and obliquely. Brain, Behavior and Evolution 77:147–158.

Fernández-Juricic, E., A. Ojeda, M. Deisher, B. Burry, P. Baumhardt, A. Stark, A. G. Elmore, and A. L. Ensminger (2013). Do male and female cowbirds see their world differently? Implications for sex differences in the sensory system of an avian brood parasite. Plos One 8:e58985.

Garza-Gisholt, E., J. M. Hemmi, N. S. Hart, and S. P. Collin (2014). A comparison of spatial analysis methods for the construction of topographic maps of retinal cell density. Plos One 9:e93485.

Glaser, E. M., and P. D. Wilson (1998). The coefficient of error of optical fractionator population size estimates: A computer simulation comparing three estimators. Journal of Microscopy 192:163–171.

Goller, B., B. F. Blackwell, T. L. DeVault, P. Baumhardt, and E. Fernández-Juricic (2018). A novel approach to assessing bird avoidance of high-contrast lights with implications for reducing human-induced avian mortality. PeerJ 6:e5404.

Govardovskii, V. I., N. Fyhrquist, T. Reuter, D. G. Kuzmin, and K. Donner (2000). In search of the visual pigment template. Visual Neuroscience 17:509–528.

Guillemain, M., G. R. Martin, and H. Fritz (2002). Feeding methods, visual fields and vigilance in dabbling ducks (Anatidae). Functional Ecology 16:522–529.

Gundersen, H. J. G. (1977). Notes on the estimation of the numerical density of arbitrary profiles: The edge effect. Journal of Microscopy 111:219–223.

Hart, N. S. (2001a). The visual ecology of avian photoreceptors. Progress in Retinal and Eye Research 20:675–703.

Hart, N. S. (2001b). Variations in cone photoreceptor abundance and the visual ecology of birds. Journal of Comparative Physiology. A, Sensory, Neural, and Behavioral Physiology 187:685–697.

Hart, N. S. (2002). Vision in the Peafowl (Aves: *Pavo cristatus*). The Journal of Experimental Biology 205:3925–3935.

Hart, N. S. (2004). Microspectrophotometry of visual pigments and oil droplets in a marine bird, the Wedge-tailed Shearwater *Puffinus pacificus*: Topographic variations in photoreceptor spectral characteristics. The Journal of Experimental Biology 207:1229–1240.

Hart, N. S., and D. M. Hunt (2007). Avian visual pigments: Characteristics, spectral tuning, and evolution. The American Naturalist 169(Suppl 1):S7–26.

Hart, N. S., and M. Vorobyev (2005). Modelling oil droplet absorption spectra and spectral sensitivities of bird cone photoreceptors. Journal of Comparative Physiology. A, Neuroethology, Sensory, Neural, and Behavioral Physiology 191:381–392.

Hart, N., J. Partridge, and I. Cuthill I (1998). Visual pigments, oil droplets and cone photoreceptor distribution in the European Starling (*Sturnus vulgaris*). The Journal of Experimental Biology 201(Pt 9):1433–1446.

Hart, N. S., J. C. Partridge, and I. C. Cuthill (1999). Visual pigments, cone oil droplets, ocular media and predicted spectral sensitivity in the Domestic Turkey (*Meleagris gallopavo*). Vision Research 39:3321–3328.

Hart, N. S., J. C. Partridge, A. T. Bennett, and I. C. Cuthill (2000a). Visual pigments, cone oil droplets and ocular media in four species of estrildid finch. Journal of Comparative Physiology. A, Sensory, Neural, and Behavioral Physiology 186:681–694.

Hart, N. S., J. C. Partridge, I. C. Cuthill, and A. T. Bennett (2000b). Visual pigments, oil droplets, ocular media and cone photoreceptor distribution in two species of passerine bird: The Blue Tit (*Parus caeruleus* L.) and the Blackbird (*Turdus merula* L.). Journal of Comparative Physiology. A, Sensory, Neural, and Behavioral Physiology 186:375–387.

Hart, N. S., J. K. Mountford, W. I. L. Davies, S. P. Collin, and D. M. Hunt (2016). Visual pigments in a palaeognath bird, the Emu *Dromaius novaehollandiae*: Implications for spectral sensitivity and the origin of ultraviolet vision. Proceedings of the Royal Society B: Biological Sciences 283:1063.

Håstad, O., J. C. Partridge, and A. Odeen (2009). Ultraviolet photopigment sensitivity and ocular media transmittance in gulls, with an evolutionary perspective. Journal of Comparative Physiology. A, Neuroethology, Sensory, Neural, and Behavioral Physiology 195:585–590.

Hawryshyn, C. W., B. R. Chou, and R. D. Beauchamp (1985). Ultraviolet transmission by the ocular media of goldfish: Implications for ultraviolet photosensitivity in fishes. Canadian Journal of Zoology 63:1244–1251.

Heesy, C. P. (2009). Seeing in stereo: The ecology and evolution of primate binocular vision and stereopsis. Evolutionary Anthropology 18:21–35.

Hodos, W. (2012). What birds see and what they don't. In How Animals See the World: Comparative Behavior, Biology, and Evolution of Vision (O.F. Lazareva, T. Shimizu, and E.A. Wasserman, Editors). Oxford University Press, Oxford, UK.

Hughes, A. (1979). A schematic eye for the rat. Vision Research 19:569–588.

Jane, S. D., and J. K. Bowmaker (1988). Tetrachromatic color vision in the duck (*Anas platyrhynchos* L.): Microspectrophotometry of visual pigments and oil droplets. Journal of Comparative Physiology A 162:225–235.

Johnsen, T. S., J. D. Hengeveld, J. L. Blank, K. Yasukawa, and V. Nolan Jr (1996). Epaulet brightness and condition in female Red-winged Blackbirds. The Auk 113:356–362.

Knott, B., J. K. Bowmaker, M. L. Berg, and A. T. Bennett (2012). Absorbance of retinal oil droplets of the budgerigar: Sex, spatial and plumage morph-related variation. Journal of Comparative Physiology. A, Neuroethology, Sensory, Neural, and Behavioral Physiology 198:43–51.

Knott, B., M. L. Berg, E. R. Morgan, K. L. Buchanan, J. K. Bowmaker, and A. T. D. Bennett (2010). Avian retinal oil droplets: Dietary manipulation of colour vision? Proceedings of the Royal Society B: Biological Sciences 277:953–962.

Knott, B., W. I. Davies, L. S. Carvalho, M. L. Berg, K. L. Buchanan, J. K. Bowmaker, A. T. Bennett, and D. M. Hunt (2013). How parrots see their colours: Novelty in the visual pigments of *Platycercus elegans*. The Journal of Experimental Biology 216:4454–4461.

Liebman, P. A. (1972). Microspectrophotometry of photoreceptors. Handbook of Sensory Physiology 2:481–528.

Linz, G. M., M. L. Avery, and R. A. Dolbeer (2017). Ecology and Management of Blackbirds (Icteridae) in North America. CRC Press, Boca Raton, FL, USA.

Lipetz, L. E. (1984). A new method for determining peak absorbance of dense pigment samples and its application to the cone oil droplets of *Emydoidea blandingii*. Vision Research 24:597–604.

Maia, R., C. M. Eliason, P. P. Bitton, S. M. Doucet, and M. D. Shawkey (2013). Pavo: An R package for the analysis, visualization and organization of spectral data. Methods in Ecology and Evolution 4:906–913.

Maier, E. J., and J. K. Bowmaker (1993). Colour vision in the passeriform bird, *Leiothrix lutea*: Correlation of visual pigment absorbance and oil droplet transmission with spectral sensitivity. Journal of Comparative Physiology A 172:295–301.

Martin, G. R. (1984). The visual fields of the Tawny Owl, *Strix aluco* L. Vision Research 24:1739–1751.

Martin, G. R. (1986). The eye of a passeriform bird, the European Starling (*Sturnus vulgaris*): Eye movement amplitude, visual fields and schematic optics. Journal of Comparative Physiology A 159:545–557.

Martin, G. R. (1993). Producing the image. In Vision, Brain and Behaviour in Birds (H. P. Zeigler and H.-J. Bischof, Editors). MIT Press, MA, USA.

Martin, G. R. (2007). Visual fields and their functions in birds. Journal of Ornithology 148(Suppl 2):S547–S562.

Martin, G. R. (2009). What is binocular vision for? A birds' eye view. Journal of Vision 9:article 14.

Martin, G. R. (2017). The Sensory Ecology of Birds. Oxford University Press, Oxford, UK.

Martin, G. R., and D. Osorio (2008). Vision in birds. In The Senses: A Comprehensive Reference. Vision 1 (A. I. Basbaum, A. Kaneko, G. M. Shepherd, and G. Westheimer, Editors). Academic Press, San Diego, CA, USA.

Martin, G. R., and S. R. Young (1983). The retinal binocular field of the pigeon (*Columba livia*: English racing homer). Vision Research 23:911–915.

McFarland, W. N., and E. R. Loew (1994). Ultraviolet visual pigments in marine fishes of the family Pomacentridae. Vision Research 34:1393–1396.

McGraw, K. J., K. Wakamatsu, A. B. Clark, and K. Yasukawa (2004). Red-winged Blackbird (*Agelaius phoeniceus*) use of carotenoid and melanin pigments to color their epaulets. Journal of Avian Biology 35:543–550.

Moore, B. A., P. Baumhardt, M. Doppler, J. Randolet, B. F. Blackwell, T. L. DeVault, E. R. Loew, and E. Fernández-Juricic (2012). Oblique color vision in an open-habitat bird: Spectral sensitivity, photoreceptor distribution and behavioral implications. The Journal of Experimental Biology 215:3442–3452.

Moore, B. A., D. Pita, L. P. Tyrrell, and E. Fernández-Juricic (2015). Vision in avian emberizid foragers: Maximizing both binocular vision and fronto-lateral visual acuity. The Journal of Experimental Biology 218:1347–1358.

Moore, B. A., L. P. Tyrrell, J. M. Kamilar, S. P. Collin, N. J. Dominy, M. I. Hall, C. P. Heesy, T. J. Lisney, E. R. Loew, G. L. Moritz, et al. (2016). Structure and function of regional specializations in the vertebrate retina. In Evolution of Nervous Systems 2e, Vol. 1 (J. Kaas, Editor). Elsevier, Oxford, UK.

Moore, B. A., L. P. Tyrrell, D. Pita, O. R. Bininda-Emonds, and E. Fernández-Juricic (2017). Does retinal configuration make the head and eyes of foveate birds move? Scientific Reports 7:38406.

Payne, R. B. (1969). Breeding seasons and reproductive physiology of Tricolored and Red-winged Blackbirds. University of California Publications in Zoology 90:1–115.

Peek, F. W. (1972). An experimental study of the territorial function of vocal and visual display in the male Red-winged Blackbird (*Agelaius phoeniceus*). Animal Behaviour 20:112–118.

Pettigrew, J. D., B. Dreher, C. S. Hopkins, M. J. McCall, and M. Brown (1988). Peak density and distribution of ganglion cells in the retinae of microchiropteran bats: Implications for visual acuity. Brain, Behavior and Evolution 32:39–56.

Porter, M. L., A. C. Kingston, R. McCready, E. G. Cameron, C. M. Hofmann, L. Suarez, G. H. Olsen, T. W. Cronin, and P. R. Robinson (2014). Characterization of visual pigments, oil droplets, lens and cornea in the Whooping Crane *Grus americana*. The Journal of Experimental Biology 217:3883–3890.

Querubin, A., H. R. Lee, J. M. Provis, and K. M. O'Brien (2009). Photoreceptor and ganglion cell topographies correlate with information convergence and high acuity regions in the adult pigeon (*Columba livia*) retina. The Journal of Comparative Neurology 517:711–722.

Raviola, E., and G. Raviola (1967). A light and electron microscopic study of the pecten of the pigeon eye. The American Journal of Anatomy 120:427–461.

Røskaft, E., and S. Rohwer (1987). An experimental study of the function of the red epaulettes and the black body colour of male Red-winged Blackbirds. Animal Behaviour 35:1070–1077.

Searcy, W. A., and K. Yasukawa (1995). Polygyny and Sexual Selection in Red-winged Blackbirds. Princeton University Press, Princeton, NJ, USA.

Sesterhenn, T. (2012). OilDropSpec (version 4.0). http://estebanfj.bio.purdue.edu/oildropspec

Siddiqi, A., T. W. Cronin, E. R. Loew, M. Vorobyev, and K. Summers (2004). Interspecific and intraspecific views of color signals in the strawberry poison frog *Dendrobates pumilio*. The Journal of Experimental Biology 207:2471–2485.

Sillman, A. J., D. A. Bolnick, L. W. Haynes, A. E. Walter, and E. R. Loew (1981). Microspectrophotometry of the photoreceptors of palaeognathous birds—The Emu and the Tinamou. Journal of Comparative Physiology A 144:271–276.

Slomianka, L., and M. J. West (2005). Estimators of the precision of stereological estimates: An example based on the CA1 pyramidal cell layer of rats. Neuroscience 136:757–767.

Smith, D. G. (1972). The role of the epaulets in the Red-winged Blackbird (*Agelaius phoeniceus*) social system. Behaviour 41:251–268.

Sokolov, E. N., J. A. Spinks, R. Näätänen, and H. Lyytinen (2002). The Orienting Response in Information Processing. Lawrence Erlbaum Associates, Mahwah, NJ, USA.

Stone, J. (1981). The Wholemount Handbook: A Guide to the Preparation and Analysis of Retinal Wholemounts. Maitland Publishing, Sydney, Australia.

Tanaka, K. D. (2015). A colour to birds and to humans: Why is it so different? Journal of Ornithology 156(Suppl 1):S433–S440.

Toomey, M. B., and J. C. Corbo (2017). Evolution, development and function of vertebrate cone oil droplets. Frontiers in Neural Circuits 11:97.

Tyrrell, L. P., and E. Fernández-Juricic (2017a). The Hawk-eyed Songbird: Retinal morphology, eye shape, and visual fields of an aerial insectivore. The American Naturalist 189:709–717.

Tyrrell, L. P., and E. Fernández-Juricic (2017b). Avian binocular vision: It's not just about what birds can see, it's also about what they can't. Plos One 12:e0173235.

Tyrrell, L. P., B. A. Moore, C. Loftis, and E. Fernández-Juricic (2013). Looking above the prairie: Localized and upward acute vision in a native grassland bird. Scientific Reports 3:3231.

Ullmann, J. F., B. A. Moore, S. E. Temple, E. Fernández-Juricic, and S. P. Collin (2012). The retinal wholemount technique: A window to understanding the brain and behaviour. Brain, Behavior and Evolution 79:26–44.

Vorobyev, M., and D. Osorio (1998). Receptor noise as a determinant of colour thresholds. Proceedings of the Royal Society B: Biological Sciences 265:351–358.

West, M. J., L. Slomianka, and H. J. Gundersen (1991). Unbiased stereological estimation of the total number of neurons in the subdivisions of the rat hippocampus using the optical fractionator. The Anatomical Record 231:482–497.

Williams, D. R., and N. J. Coletta (1987). Cone spacing and the visual resolution limit. Journal of the Optical Society of America. A, Optics and Image Science 4:1514–1523.

Wright, M. W., and J. K. Bowmaker (2001). Retinal photoreceptors of paleognathous birds: the Ostrich (*Struthio camelus*) and Rhea (*Rhea americana*). Vision Research 41:1–12.

Yasukawa, K., L. K. Butler, and D. A. Enstrom (2009b). Intersexual and intrasexual consequences of epaulet colour in male Red-winged Blackbirds: An experimental approach. Animal Behaviour 77:531–540.

Yasukawa, K., D. A. Enstrom, P. G. Parker, and T. C. Jones (2009a). Epaulet color and sexual selection in the Red-winged Blackbird: A field experiment. The Condor 111:740–751.

Yasukawa, K., D. A. Enstrom, P. G. Parker, and T. C. Jones (2010). Male Red-winged Blackbirds with experimentally dulled epaulets experience no disadvantage in sexual selection. Journal of Field Ornithology 81:31–41.

Yasukawa, K. and W. A. Searcy (1995). Red-winged Blackbird (*Agelaius phoeniceus*), version 2.0. In The Birds of North America (A. F. Poole and F. B. Gill, Editors). Cornell Lab of Ornithology, Ithaca, NY, USA. https://doi-org/10.2173/bna.184.

Yokoyama, S., N. S. Blow, and F. B. Radlwimmer (2000). Molecular evolution of color vision of Zebra Finch. Gene 259:17–24.

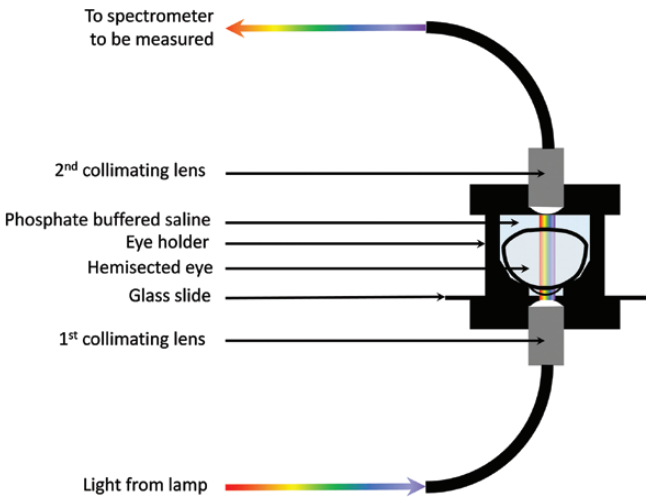

APPENDIX FIGURE 8. Diagram of setup used for the measurement of ocular media transmittance. Multicolored rectangle and arrows represent the light path through the setup. Diagram not to scale.

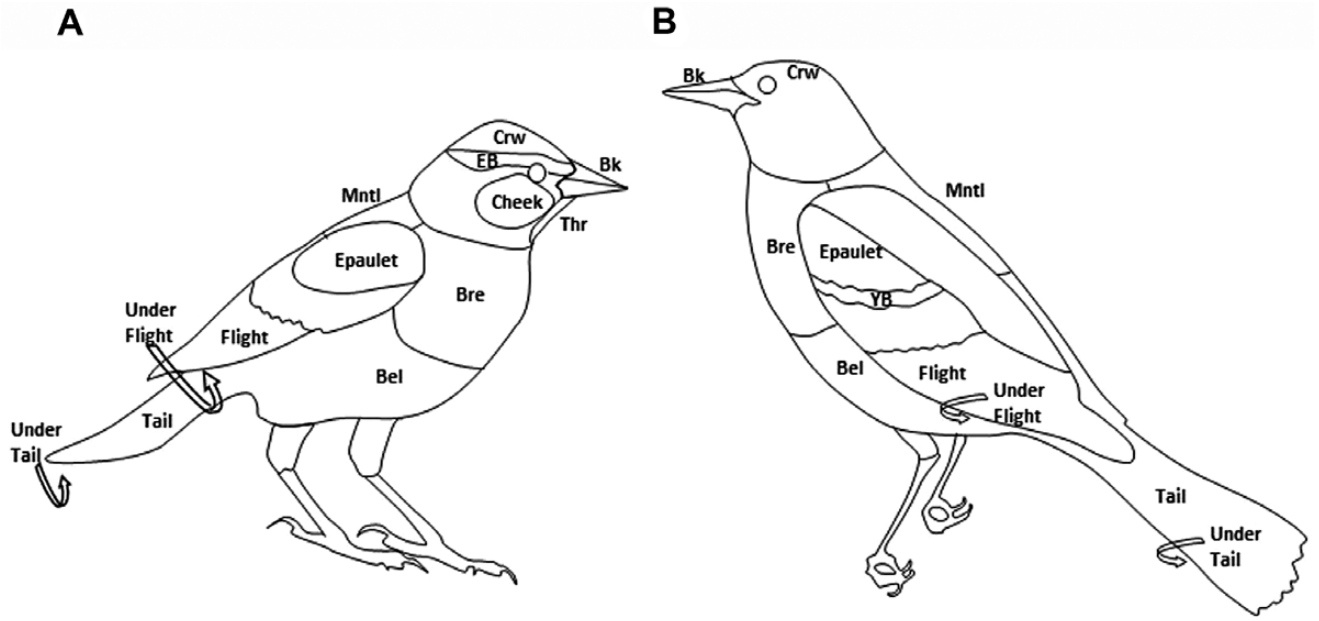

APPENDIX FIGURE 9. Plumage patches of **(A)** female and **(B)** male Red-winged Blackbird used in contrast calculations. Bk = beak, Bel = belly, Bre = breast, Cheek, Crw = crown, Epaulet, EB = eye bar, Flight = distal side of flight feathers, Mntl = mantle, Tail = dorsal side of tail feathers, Thr = throat, Under Flight = proximal side of flight feathers, Under Tail = ventral side of tail feathers, and YB = Yellow wing bar. Images not to scale.

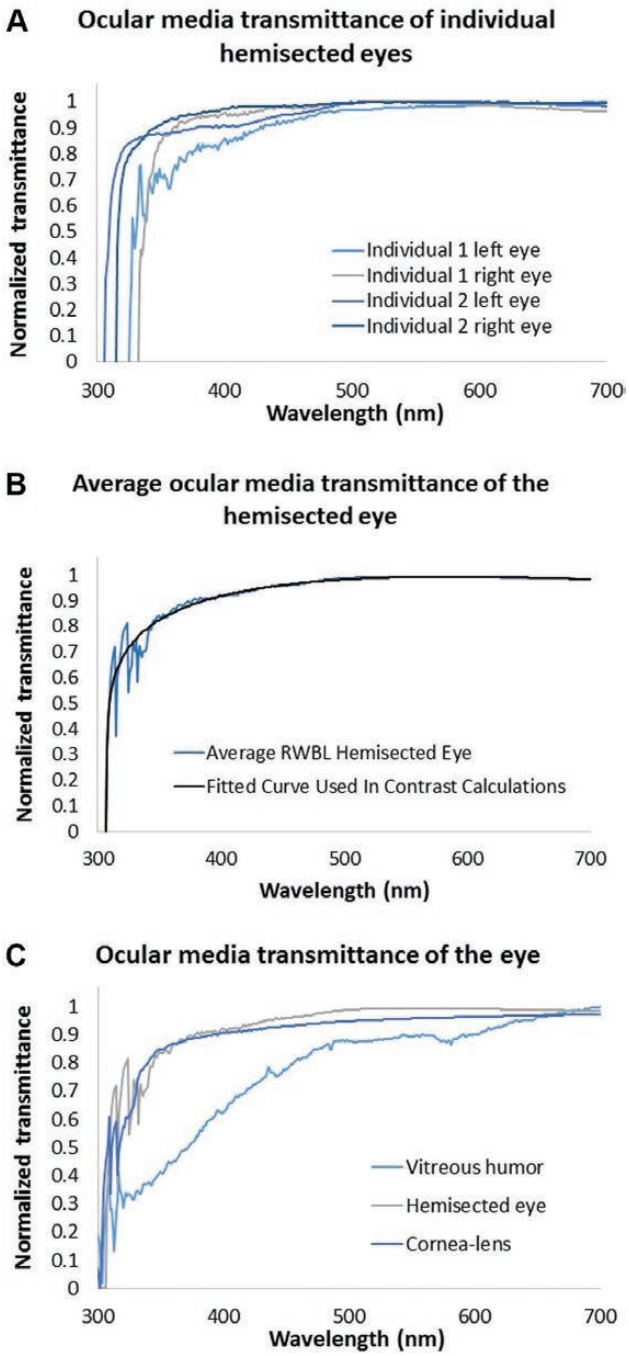

APPENDIX FIGURE 10. Normalized transmittance spectra of the Red-winged Blackbird ocular media: (**A)** 4 individual hemisected eyes measured; **(B)** average transmittance spectra of the hemisected eye and the fitted curve used in the plumage contrast calculations; **(C)** average transmittance spectra of the hemisected eye, cornea-lens, and vitreous humor.

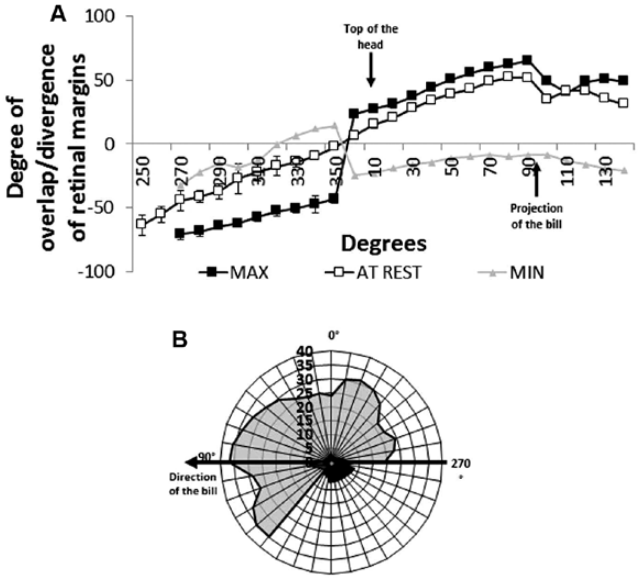

APPENDIX FIGURE 11. **(A)** Degree of overlap (mean ± SE) of the retinal margins of Red-winged Blackbirds along different elevations measured at the median sagittal plane when eyes were at rest (white squares), converged (black squares), and diverged (grey triangles). Positive values indicate binocular overlap, while negative values indicate blind areas. **(B)** Degree of eye movement along the median sagittal plane.

APPENDIX TABLE 2. Parameters used for the calculation of both the Scheaffer-Mendenhall-Ott coefficient of error (SMO CE) and the SMO CE^2/CV^2 (CV = coefficient of variation) reliability estimates for all retinas used to calculate retinal ganglion cell (RGC) and photoreceptor (PH) density.

Retina no.	Cells counted (*n*)	SD of the cells counted	Sites counted (*n*)	Mean cells per site (*n*)	Variance	SMO CE	CV	SMO CE^2/CV^2
RGC 1	11,112	17.6	360	30.9	265.3	0.0257	0.570	0.00203
RGC 2	12,871	24.6	340	37.9	510.8	0.0295	0.650	0.00206
RGC 3	15,067	22.4	387	38.9	473.8	0.0276	0.576	0.00230
RGC 4	15,180	23.5	375	40.5	510.2	0.0276	0.581	0.00226
RGC 5	16,828	29.8	365	46.1	785.0	0.0299	0.647	0.00214
PH 6	15,354	32.9	224	68.5	739.3	0.0219	0.480	0.00209
PH 7	14,745	35.3	155	95.1	756.0	0.0181	0.371	0.00238
PH 8	12,277	23.0	186	66.0	379.0	0.0183	0.349	0.00275

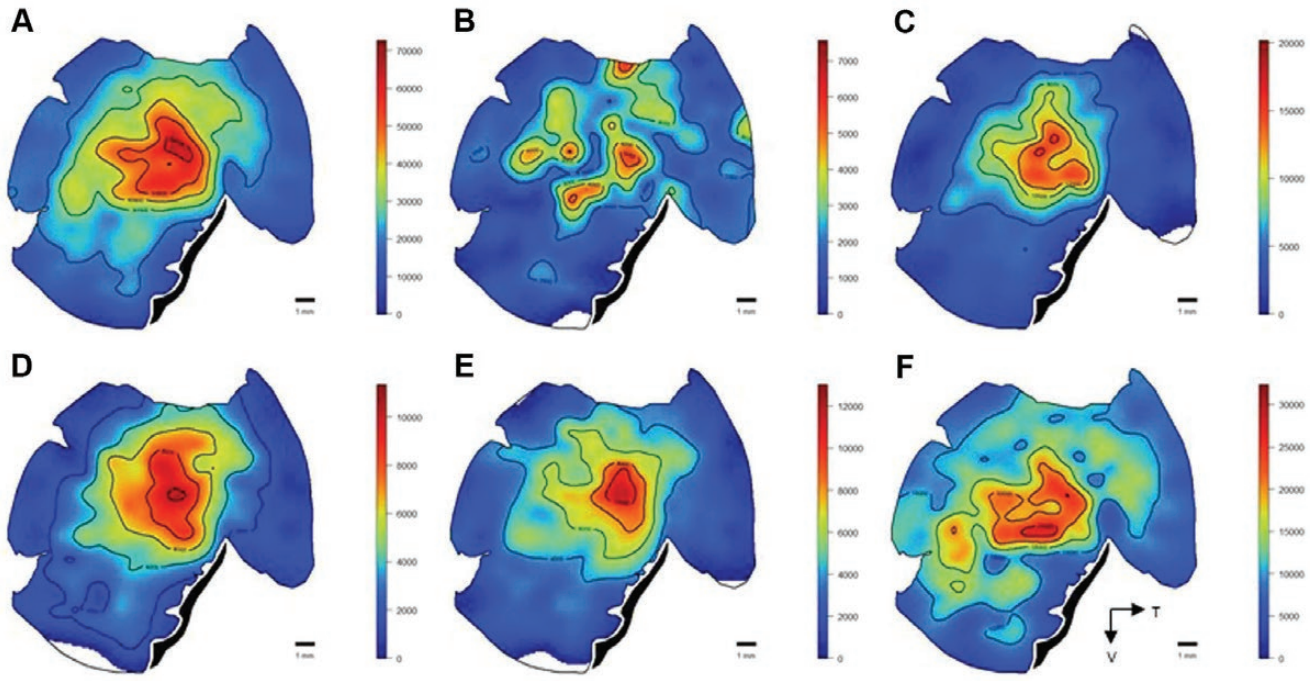

APPENDIX FIGURE 12. Cone photoreceptor topographic maps representing the Red-winged Blackbird retina: **(A)** all photoreceptors, **(B)** UVS single cone (T-Type oil droplet), **(C)** SWS single cone (C-Type oil droplet), **(D)** MWS single cone (Y-Type oil droplet), **(E)** LWS single cone (R-Type oil droplet), and **(F)** double cone (P-Type oil droplet). Isodensity lines connect areas of similar density (cells mm^{-2}) of cones across the retina. T = Temporal; V = Ventral. Pecten location is indicated by a black streak.

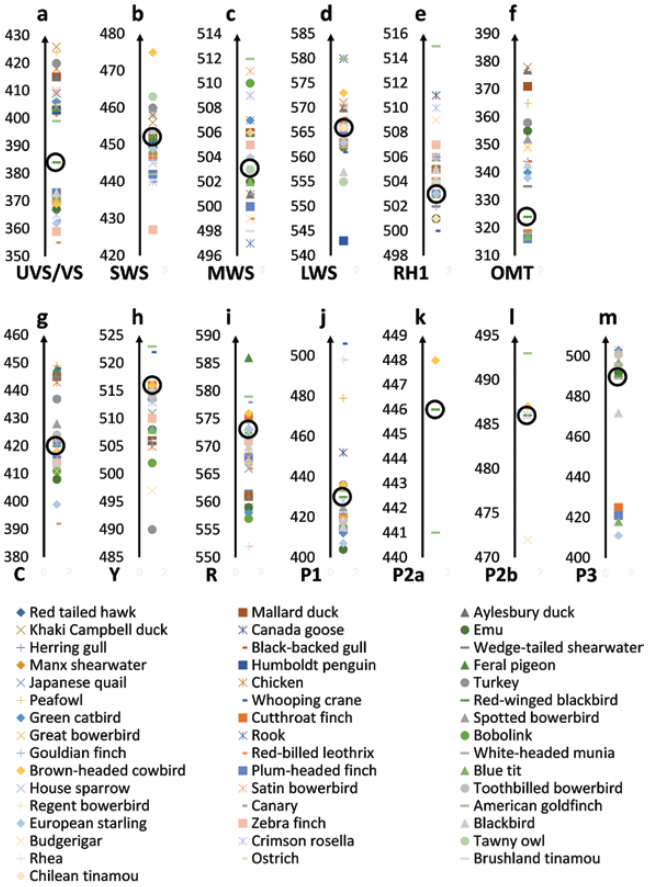

APPENDIX FIGURE 13. Photoreceptor visual pigment (λ_{max}), oil droplet (λ_{cut}), and ocular media transmittance ($\lambda_{T0.5}$) lambda parameters for all species where microspectrophotometric data are published. Red-winged Blackbird marked with black circle. **(A)** UVS/VS cone photoreceptor, **(B)** SWS cone photoreceptor, **(C)** MWS cone photoreceptor, **(D)** LWS cone photoreceptor, **(E)** RH1 rod photoreceptor, **(F)** ocular media transmittance (OMT), **(G)** C-Type oil droplet, **(H)** Y-Type oil droplet, **(I)** R-Type oil droplet, **(J)** P1-Type oil droplet, P2-Type oil droplet a **(K)** and b **(L)** peaks, and **(M)** P3-Type oil droplet. See Appendix Table 3 for order, scientific name, common name, and reference of all species.

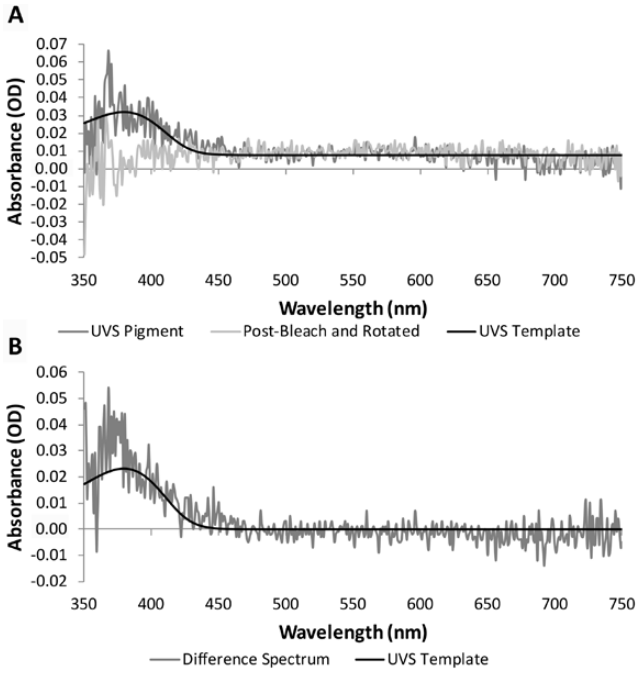

APPENDIX FIGURE 14. Exemplar UVS visual pigment absorbance spectra. **(A)** UVS visual pigment absorbance curve (dark grey) with post-bleach and rotated spectrum (grey), with the black line indicating a 380 nm A1-rhodopsin template from Govardovskii et al. (2000). **(B)** Difference spectrum (dark grey) between the UVS visual pigment absorbance curve and post-bleach and rotated spectrum in panel (**A**), with the black line indicating a 380 nm A1-rhodopsin template from Govardovskii et al. (2000).

APPENDIX TABLE 3. Order, scientific name, common name, and reference of species data used in Appendix Figure 13.

Order	Scientific name	Common name	Reference
Accipitriformes	*Buteo jamaicensis*	Red-tailed Hawk	Sillman et al. (1981)
Anseriformes	*Anas platyrhynchos*	Mallard Duck	Jane and Bowmaker (1988)
Anseriformes	*A. platyrhynchos dom.*	Aylesbury Duck	Jane and Bowmaker (1988)
Anseriformes	*A. platyrhynchos dom.*	Khaki Campbell Duck	Jane and Bowmaker (1988)
Anseriformes	*Branta canadensis*	Canada Goose	Moore et al. (2012)
Casuariiformes	*Dromaius novaehollandiae*	Emu	Hart et al. (2016)
Charadriiformes	*Larus argentatus*	Herring Gull	Håstad et al. (2009)
Charadriiformes	*L. marinus*	Black-backed Gull	Håstad et al. (2009)
Ciconiiformes	*Puffinus pacificus*	Wedge-tailed Shearwater	Hart (2004)
Ciconiiformes	*P. puffinus*	Manx Shearwater	Bowmaker et al. (1997)
Ciconiiformes	*Spheniscus humboldti*	Humboldt Penguin	Bowmaker and Martin (1985)
Columbiformes	*Columba livia*	Feral Pigeon	Bowmaker et al. (1997)
Galliformes	*Coturnix coturnix japonica*	Japanese Quail	Bowmaker et al. (1993)
Galliformes	*Gallus gallus dom.*	Chicken	Bowmaker et al. (1997)
Galliformes	*Meleagris gallopavo*	Turkey	Hart et al. (1999)
Galliformes	*Pavo cristatus*	Peafowl	Hart (2002)
Gruiformes	*Grus americana*	Whooping Crane	Porter et al. (2014)
Passeriformes	*Agelaius phoeniceus*	Red-winged Blackbird	Present study
Passeriformes	*Ailuroedus crassirostris*	Green Catbird	Coyle et al. (2012)
Passeriformes	*Amadina fasciata*	Cutthroat Finch	Hart et al. (2000a)
Passeriformes	*Chlamydera maculata*	Spotted Bowerbird	Coyle et al. (2012)
Passeriformes	*C. nuchalis*	Great Bowerbird	Coyle et al. (2012)
Passeriformes	*Corvus frugilegus*	Rook	Bowmaker (1979)
Passeriformes	*Dolichonyx oryzivorus*	Bobolink	Beason and Loew (2008)
Passeriformes	*Erythrura gouldiae*	Gouldian Finch	Hart et al. (2000a)
Passeriformes	*Leothrix lutea*	Red-billed Leothrix	Maier and Bowmaker (1993)
Passeriformes	*Lonchura maja*	White-headed Munia	Hart et al. (2000a)
Passeriformes	*Molothrus ater*	Brown-headed Cowbird	Fernández-Juricic et al. (2013)
Passeriformes	*Neochmia modesta*	Plum-headed Finch	Hart et al. (2000a)
Passeriformes	*Cyanistes caeruleus*	Blue Tit	Hart et al. (2000b)
Passeriformes	*Passer domesticus*	House Sparrow	Hart and Hunt (2007)
Passeriformes	*Ptilonorhynchus violaceus*	Satin Bowerbird	Coyle et al. (2012)
Passeriformes	*Scenopooetes dentirostris*	Toothbilled Bowerbird	Coyle et al. (2012)
Passeriformes	*Sericulus chrysocephalus*	Regent Bowerbird	Coyle et al. (2012)
Passeriformes	*Serinus canaria*	Canary	Das et al. (1999)
Passeriformes	*Spinus tristis*	American Goldfinch	Baumhardt et al. (2014)
Passeriformes	*Sturnus vulgaris*	European Starling	Hart et al. (1998)
Passeriformes	*Taeniopygia guttata*	Zebra Finch	Bowmaker et al. (1997), Yokoyama et al. (2000)
Passeriformes	*Turdus merula*	Blackbird	Hart et al. (2000b)
Psittaciformes	*Melopsittacus undulatus*	Budgerigar	Bowmaker et al. (1997), Knott et al. (2012)
Psittaciformes	*Platycercus elegans*	Crimson Rosella	Knott et al. (2010), Carvalho et al. (2011), Knott et al. (2013)
Strigiformes	*Strix aluco*	Tawny Owl	Bowmaker and Martin (1978)
Struthioniformes	*Rhea Americana*	Rhea	Wright and Bowmaker (2001)
Struthioniformes	*Struthio camelus*	Ostrich	Wright and Bowmaker (2001)
Tinamiformes	*Nothoprocta cinerascens cinerascens*	Brushland Tinamou	Sillman et al. (1981)
Tinamiformes	*Nothoprocta perdicaria sanborni*	Chilean Tinamou	Sillman et al. (1981)